Grad-Shafranov Reconstruction Of Magnetic Flux Ropes

The Influence Of The Boundary Selection On The Reconstruction

Tom Eynard-Machet

May 26, 2021

Tom Eynard-Machet, BSc

Grad-Shafranov Reconstruction of Magnetic Flux Ropes: The Influence of the Boundary Selection on the Reconstruction

MASTER'S THESIS

to achieve the university degree of

Master of Science

Master's degree programme: Physics

submitted to

Graz University of Technology

Supervisor

Assoc. Prof. Mag. Dr. rer. nat. Manuela Temmer

Institut für Physik, Institutsbereich Geophysik, Astrophysik und Meteorologie, NAWI Graz, University of Graz, Universitätsplatz 5/II, 8010 Graz, Austria.

Graz, Mai 2021

Tom Eynard-Machet

Grad-Shafranov Reconstruction Of Magnetic Flux Ropes – The Influence Of The Boundary Selection On The Reconstruction

Thesis in partial fulfillment of the requirements for the degree of MSc;
Thesis submitted on Mai 26, 2021 and defended on July 2, 2021.

Department for Geophysics, Astrophysics and Meteorology,
Institute for Physics, NAWI Graz, University of Graz.

Supervisors: Assoc. Prof. Mag. Dr. rer. nat. Manuela Temmer[1]

[1] Institut für Physik, Institutsbereich Geophysik, Astrophysik und Meteorologie,
   NAWI Graz, University of Graz, Universitätsplatz 5/II, 8010 Graz, Austria.

Abstract

Aims. In this thesis, we explore the Grad-Shafranov method to reconstruct magnetic flux ropes. The goal is to determine the influence of the selection of the cloud boundaries on the output of the reconstruction. Moreover, we study the impact of the smoothing on the reconstruction. Finally, we try to evaluate the sensitivity of the reconstruction procedure.

Methods. We are using the new MATLAB code written by Qiang Hu to reconstruct 17 times the magnetic cloud detected on 2013-06-28. For each reconstruction, we modify the boundaries and analyse the differences in the output parameters of the reconstruction. We also repeat the 17 reconstructions with smoothed data and compare these results with the literature. At last, we compare seven reconstructions of the same event and vary the input parameters to investigate the robustness of the code.

Results. A variation of one minute on the front boundary has an average influence three to four times greater than an equal variation of the rear boundary on the output parameters. However, the uncertainty on the location of the front boundary is almost four times lower than the one of the rear boundary. The study on smoothed data leads to similar results. The results of the 17 reconstructions deviate from those of the literature by 10.2% and 0.7% for the unsmoothed and smoothed data respectively. Finally, seven reconstructions do not represent a statistically large enough sample size and, therefore, do not allow to draw a conclusion on the robustness of the code.

Keywords: Space weather; Solar physics; CMEs; Magnetic field

Acknowledgement

Contents

Introduction

The Sun dictates our sleep, our mood, and provides a fix point to measure our time on Earth. As a physicist, the Sun is the greatest laboratory in our reach. The most energetic events and violent phenomena take place in, on, and around the Sun.

Due to the Sun, the effects of general relativity have been observed. We received, from stars, photons that have been deflected by the curved space-time in the surroundings of the Sun. In addition, some fundamental theoretical progress has been made observing the Sun. As an example, we can cite the neutrino problem. In fact, the number of neutrinos coming from the Sun represented a third of the predicted neutrinos. This observation led, in turn, to the discovery of the oscillation of neutrinos. Furthermore, quantum mechanics are involved as it allows the fusion to occur in the core of the Sun. During the fusion process, the energy produced is radiated and transported through the different layers of the Sun. The energy is carried away through radiative energy transport or convective energy transport. Overall, the Sun unites a large scope of physical topics.

The Sun is hot enough to ionise the atoms and create plasma, whose motion creates an electromagnetic field. The convection in the Sun coupled with its differential rotation generate a solar activity cycle with a period of 22 years (Balogh et al., 2015). The magnetic field lines can be either open or closed. The open magnetic field lines are associated with coronal holes. These are regions of lower density and temperature where the plasma is accelerated to high velocities and expelled in the interplanetary medium. This high speed stream is known as fast solar wind, in opposition to slow solar wind associated with the expansion of the solar corona. The coronal holes usually situate at high latitudes, but can move towards lower latitudes during high solar activity, creating a higher pressure on the Earth's magnetic field. Closed magnetic field lines are dragged by the plasma on the surface of the Sun. Some of them carry plasma up to the solar corona. The differential rotation is creating torsion, shearing and twisting of the closed magnetic field lines, storing energy. When the balance breaks down, the magnetic field lines reconnect and release this energy, triggering an eruptive event. The plasma, along with the magnetic field, is ejected into the interstellar medium at high speeds. This event is called a Coronal Mass Ejection (CME) (Balogh et al., 2015). Eventually, this magnetic ejecta, also called magnetic cloud, will propagate towards the Earth. A magnetic flux rope expands alongside the core of the magnetic cloud. The latter is defined as a group of magnetic field lines twisting around a common axis (Lowder and Yeates, 2017). The Global Geospace Science WIND satellite, launched in 1994, measures, among others, the magnetic field, plasma temperature, plasma density and plasma velocity at the Lagrange point L1 (NASA et al., 2021). At

this point L1, the satellite is situated on the day side of the Earth, allowing measurements without interruptions. The database of CDAWeb (`https://cdaweb.gsfc.nasa.gov/index.html/`) gives an access to the measurements of WIND's instrumentations. With these tools, we can have an insight in the physics that happens in the magnetic ejecta reaching the Earth. Several methods are modelling the magnetic flux ropes. The Lundquist (1950) or the Gold-Hoyle (1960) methods have been able to apprehend and reconstruct the shape of the magnetic flux ropes. More recently, the Grad-Shafranov method has been used to reconstruct these clouds. Originally used to reconstruct the interaction between the solar wind and the Earth's magnetopause, it is now efficient in reconstructing the magnetic clouds themselves (Möstl et al., 2009). Unlike the Lundquist and Gold-Hoyle methods, the Grad-Shafranov method does not make assumptions about the shape of the magnetic field components, but uses the symmetries of the magnetic flux ropes as a base for the reconstruction. However, with the measured magnetic fields, the boundaries of the flux ropes are not well defined and have yet to be tested.

In this master thesis, I will describe the Grad-Shafranov method and discuss the influence of the choice of the magnetic flux rope's boundaries on the reconstruction. At first, I will summarize the state of our knowledge of the Sun and its activity. It is followed by an explanation why this activity is at the origin of the propagation of magnetic flux ropes in the interstellar medium. Thereafter, I will present the Grad-Shafranov reconstruction method and apply it on an example. Additionally, the choice of the boundaries of the magnetic flux rope is going to be discussed through a set of reconstructions of the same event. Finally, I am going to test the robustness of the code by reconstructing several times the same magnetic flux rope with identical boundaries.

The Sun and its activity

<div style="text-align: right">2</div>

In order to understand the importance and the origin of the study of magnetic clouds, it is necessary to recall some knowledge that we have on the Sun. In this section, I will start by describing the Sun in its entirety and explain the origin of its magnetic field. Then, I will define what solar winds, CMEs and magnetic flux ropes are and enumerate their characteristics. Lastly, I will attempt to summarize the impacts that the Sun's activity has on the Earth.

2.1 The sun as a star

2.1.1 The sun in the galaxy

The Sun seems enormous to us, containing 99.8% of the mass of our solar system. In the spectrum of the stars we know, the Sun is considered a Yellow Dwarf (NASA, 2019), even though it is heavier than 93.9% of the stars in our galaxy (Kroupa, 2000). Moreover, it is possible to classify the Sun according to the Harvard classification of stars. This classification has been created to describe easily, but efficiently the stars according to their emission and absorption lines (Jaschek and Jaschek, 1987). On the other hand, each type of star has its temperature range. An analysis of the blackbody spectrum of the star should be, therefore, enough to classify the star (as given in table. 2.1) (Habets and Heintze, 1981).

Star Type	Temperature (Kelvin)
O	≥ 30 000K
B	10 000 - 30 000K
A	7 500 - 10 000K
F	6 000 - 7 500K
G	5 200 - 6 000K
K	3 700 - 5 200K
M	32 400 - 3 700K

Table 2.1: Correspondence between the type of a star and its effective temperature.

In this table, it is easy to see that the Sun, with its effective temperature of 5772K, is a G type star (Mamajek et al., 2015; Habets and Heintze, 1981). In fact, knowing its temperature and its age, it is possible to characterize the Sun as a G2V star. The V means that the Sun is

on the main sequence. The evolution track of stars can be seen in the Herzsprung Russel Diagram (figure 2.1). This diagram displays the relative luminosity with respect to the color index, which yields a single Planck curve equivalent to a temperature.

Stars are often created from the contraction of an interstellar cloud, that may be the remnant of a supernova. Once the protostar is created, accretion of mass increases the mass of the star. Eventually, if the internal pressure of the object is high enough, fusion processes occur. The main fusion process is known as proton-proton chain (or pp-chain) and is considered as the beginning of the main sequence (Karttunen et al., 2017). A star leaves the main sequence when the Hydrogen in its core is exhausted. Then, the radiation pressure does not counteract the gravitational pressure, and the star collapses. For large stars, the collapse can result in a black hole or a neutron star, whereas lighter ones will mainly end in white dwarfs. Furthermore, light stars burn their Hydrogen slower than massive ones. There is a strong correlation between mass and life expectancy. We can read it in the figure 2.2 (Karttunen et al., 2017; Bertulani, 2013). The Sun should live approximately 10 Gy (10^9 years). Its actual age can be calculated with the help of helioseismology, which yields an age of 4.6 Gy, also corresponding to the age of the oldest meteorite (Dziembowski et al., 1998). The same age, 4.567 ± 0.0003 Gy, has been predicted by the study of Calcium-Aluminium-rich Inclusion (CAI) in primitive meteorites (Bizzarro et al., 2012). Furthermore, the mass of the Sun can be calculated with the third Kepler's law and has a value of 1.327 10^{20}m^3 s^{-2} (GM), meaning a mass of 1.98 10^{30} kg (Luzum et al., 2011; Mamajek et al., 2015). Finally, the radius of the Sun is 695660 km according to both seismic and photospheric studies (Haberreiter et al., 2008).
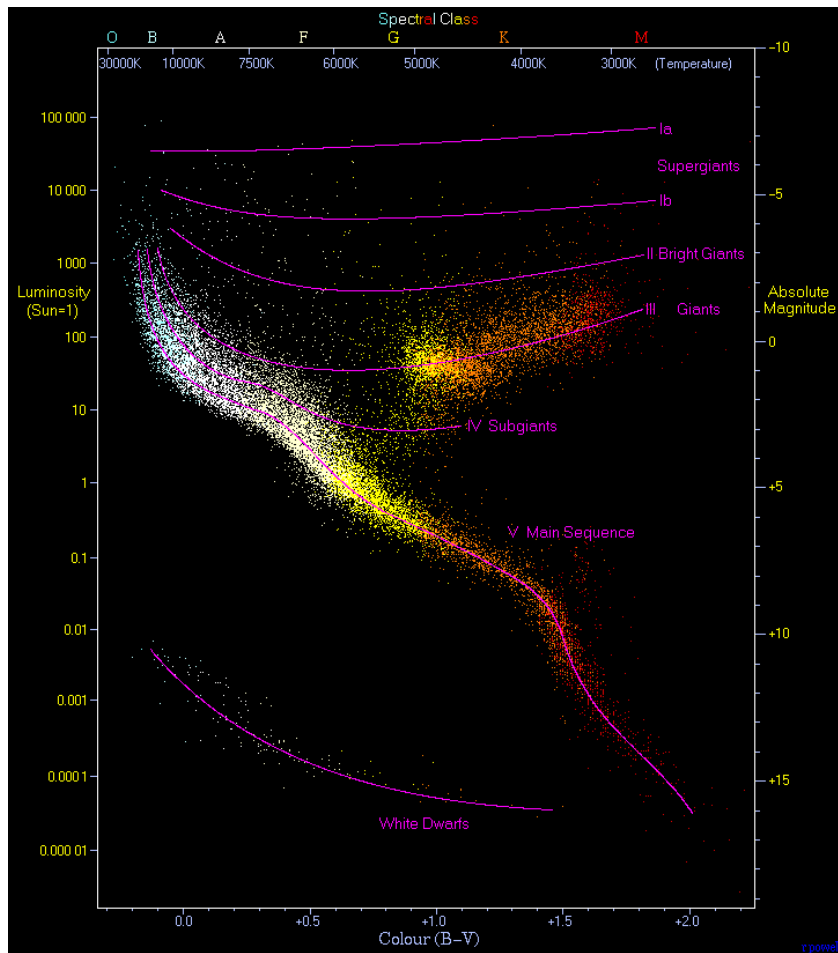
Fig. 2.1: Herzsprung Russel Diagram of 22 000 stars from Hipparcos Catalogue (Powell, 2011).

Mass (solar masses)	Time (years)	Spectral type
60	3 million	O3
30	11 million	O7
10	32 million	B4
3	370 million	A5
1.5	3 billion	F5
1	10 billion	G2 (Sun)
0.1	1000s billions	M7

Table 2.2: Life expectancy of stars with respect to their masses (Bertulani, 2013).

2.1.2 The solar interior

Now that the situation of the Sun among the other stars has been clarified, the structure of the Sun itself has to be described. We will list shortly the different layers of the solar interior and give some of their main characteristics.

The core The core of the Sun is the place where fusion processes take place. The Hydrogen fuse into Helium. This fusion process happens only because the conditions of temperature and pressure are extremes. Indeed, the density at the very center of the core is estimated at 150 g cm^{-3}, and at the transition point from core to radiation zone, it is estimated to be 20 g cm^{-3} (Basu et al., 2009). Likewise, the temperature at the very center reaches 15 million Kelvin. The NASA has released in its book "Solar Math Educator Guide" of 2013 that the density inside the Sun can be modeled by the function: $\rho(x) = 519x^4 - 1630x^3 + 1844x^2 - 889x + 155$, where x is $\frac{r}{R}$ and R is the radius of the Sun. Using the integrated mean formula 2.1, it is possible to calculate the mean value of the density between $x = 0$ and $x = 0.25$, considered here as the outer boundary of the core. This mean value equals 76.32 g cm^{-3}. The core encompasses the volume included within 25% of the total radius of the Sun (Hathaway, 2015; Christensen-Dalsgaard et al., 1996). This volume represents 1.5% of the total volume of the Sun, but according to our calculation, it should contain 84% of its mass. However, it seems like the core really contains only 50% of the total mass of the Sun (Dunbar, 2017).

$$\overline{\rho(x)} = \frac{1}{b-a} \int_a^b \rho(x)dx \qquad (2.1)$$

The radiative zone The radiative zone extends from 25% to 70% of the radius of the Sun. It is called radiative zone due to the type of energy transport that takes place in this region, called radiative transfer. Indeed, the nuclear energy created in the core is stored in photons that propagate through the radiative zone. The radiative zone contains mainly plasma. Hence, the photons can bounce and scatter with other particles (Dunbar, 2017). The path followed by such a photon is called random walk. A photon takes approximately 170 000 years to escape the Sun due to these succesive bounces (Mitalas and Sills, 1992). In fact, the mean distance that a photon can travel without encountering another particle is called mean free path, and its value is of 1.2 10^{-4} m in the solar radiative zone (Walker, 2006).

Convection does not happen in this region. First, let us imagine a "bubble" of hot matter. The bubble expands and starts to rise due to the buoyancy force. If the rate of energy exchange between the bubble and its environment is high, the hot matter will immediately cool down and sink or stabilize at its level. Here, there

is no convection. Now, if the rate of energy exchange between the bubble and its environment is low, the bubble rises, but does not cool down. It will rise until it reaches a layer with the same density, cool down, and sink again. This last process is called convection. To summarize, a high temperature gradient and a low energy dissipation lead to convective energy transport, but a low temperature gradient with a high energy dissipation creates radiative energy transport (Leblanc, 2011). The temperature gradient or the ability of a fluid to dissipate energy are both strongly linked to their capacity to absorb energy or photons. This characteristic is called opacity. In other words, if the opacity of a fluid is high, it will store the energy, create a temperature gradient and cool down slowly. On the contrary, if the opacity is low, the photons travel through the medium, creating a low temperature gradient.

The temperature of the radiation zone decreases from 7 million to 2 million Kelvin (Hathaway, 2015). Moreover, the state of the matter in this region does not allow complex molecules to keep their electrons. In turn, this means that the photons are less likely to be absorbed, meaning that the opacity is low. As we discussed, a high temperature gradient and a low opacity do not allow convection. This zone is radiative.
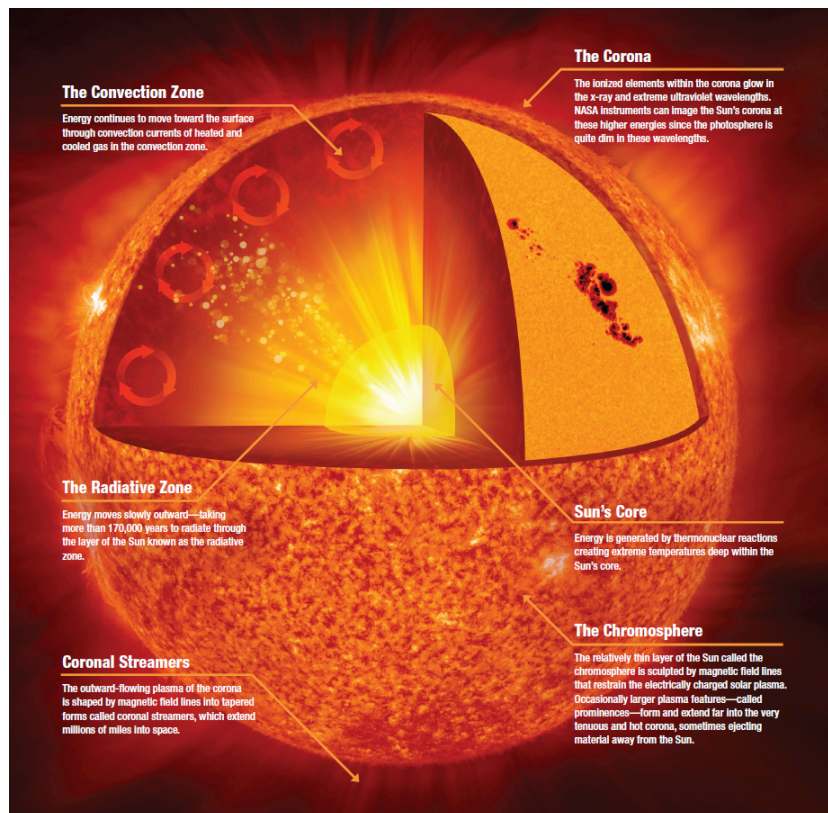
Fig. 2.2: The structure of the Sun interior (Jenny Mottar, 2017).

The convection zone The convection zone starts when the radiation zone ends. It ends near the surface of the Sun. The transition region between the radiative and the convective zone is called the tachocline. It is also the depth at which a differential rotation starts to be observed (Route, 2016). At the tachocline, the temperature is

approximately 2 million Kelvin, which is low enough for some atoms to keep their electrons bonded. Eventually, those can absorb photons and excite. This phenomenon increases the opacity of the matter, and makes it unstable (Hathaway, 2015). The temperature gradient coupled with the opacity of this region allows convection in this layer. It is probable that the motion of the ionised matter in this layer is at the origin of a strong magnetic field.

2.1.3 The solar atmosphere

The solar interior can be understood as everything that lies under the surface of the Sun. In opposition, the atmosphere represents the layers that add up above this surface. The surface is the layer where the Sun becomes optically thin. I will now describe each atmosphere layer and their characteristics.

Table 2-1: The Holweger-Müller Model Atmosphere[7]

Height[8] (km)	Optical Depth (τ_{5000})	Temperature (°K)	Pressure (dynes cm^{-2})	Electron Pressure (dynes cm^{-2})	Density (g cm^{-3})	Opacity (κ_{5000})
550	5.0×10^{-5}	4306	5.20×10^2	5.14×10^{-2}	1.90×10^{-9}	0.0033
507	1.0×10^{-4}	4368	8.54×10^2	8.31×10^{-2}	3.07×10^{-9}	0.0048
441	3.2×10^{-4}	4475	1.75×10^3	1.68×10^{-1}	6.13×10^{-9}	0.0084
404	6.3×10^{-4}	4530	2.61×10^3	2.48×10^{-1}	9.04×10^{-9}	0.012
366	0.0013	4592	3.86×10^3	3.64×10^{-1}	1.32×10^{-8}	0.016
304	0.0040	4682	7.35×10^3	6.76×10^{-1}	2.47×10^{-8}	0.027
254	0.010	4782	1.23×10^4	1.12	4.03×10^{-8}	0.040
202	0.025	4917	2.04×10^4	1.92	6.52×10^{-8}	0.061
176	0.040	5005	2.63×10^4	2.54	8.26×10^{-8}	0.075
149	0.063	5113	3.39×10^4	3.42	1.04×10^{-7}	0.092
121	0.10	5236	4.37×10^4	4.68	1.31×10^{-7}	0.11
94	0.16	5357	5.61×10^4	6.43	1.64×10^{-7}	0.14
66	0.25	5527	7.16×10^4	9.38	2.03×10^{-7}	0.19
29	0.50	5963	9.88×10^4	22.7	2.60×10^{-7}	0.34
0	1.0	6533	1.25×10^5	73.3	3.00×10^{-7}	0.80
-34	3.2	7672	1.59xe+005	551	3.24×10^{-7}	3.7
-75	16	8700	2.00xe+005	2.37×10^3	3.57×10^{-7}	12

Table 2.3: The Holweger-Müller model describing the photosphere and its boundaries (Holweger and Müller, 1974).

The photosphere The photosphere is known as the lowest atmospheric region of the Sun. The opacity changes from thick to thin within this layer (Holweger and Müller, 1974). Indeed, in the figure 2.3, we can see that the opacity becomes inferior to one between −34 km and 0 km above the surface. The photosphere extends up to 500 km above the surface of the Sun. From the same figure 2.3, we can read the temperature at each border of the photosphere (0 km and 500 km). These temperatures range from 6533 K to 4368 K. In reality, the effective temperature of the Sun has been evaluated at 5772 K from an analysis of the blackbody spectrum of the Sun (Mamajek et al., 2015). The maximum of the spectrum yields the temperature of this blackbody.

The chromosphere Literally, the word chromosphere means "the sphere of colors". This can be explained by the fact that, during solar eclipses, one can see the chromosphere with bare eyes as a pink halo that surrounds the Sun. In fact, the chromosphere is the layer where the temperature gradient reverses. Indeed, from the core to the photosphere, the temperature gradient is negative. In other words, the temperature decreases with increasing distance to the center of the Sun. The chromosphere presents a minimum temperature at its boundary with the photosphere, and then increases up to 6500 K from 1000 km to 1500 km over the surface. Higher than this plateau, the temperature increases again up to 20000 K (Thay and Thomas, 1956). Overall, the chromosphere extends up to 2000 km. The consequence of the positive temperature gradient is that instead of absorption lines, the chromosphere can be observed off-limb with its emission lines, especially the H_α line (Bray, 1973).

The transition zone The transition zone is the layer that is found between the chromosphere and the corona. It deserves to be distinguished from those two layers, because it is within this region that the temperature and the density are changing radically. While the temperature increases by a factor of 100 (from 20 000K to 2 million K), the density decreases by a factor of 100 over a distance of 500 km approximately (Golub and Pasachoff, 2010).

The corona The corona is the outermost layer of the Sun's atmosphere. It is still largely unknown nowadays. Some studies have tried to explain how the temperature could be so high in the region (Aschwanden et al., 2007). Indeed, the temperature was measured to be over one million Kelvin (Golub and Pasachoff, 2010). Nevertheless, several hypotheses like Alfvén waves heating or microflaring still try to explain it (Heyvaerts and Priest, 1983; Moore et al., 1991). The temperature and the density of the solar corona induce that the plasma should expand in the less dense interstellar medium. The tail of comets gives a clue of the presence of this expansion. This slow outflow of the corona is called the slow solar wind (Golub and Pasachoff, 2010). The interstellar medium, in which this wind is flowing is, however, not empty. It means that this wind slows down, and eventually, creates a shock that surrounds the Heliosphere. Voyager 1 crossed this termination shock on December 2004 (Stone

et al., 2005).

On the contrary, some regions of the corona are cooler and less dense than usual. In these darker regions, called coronal holes, the plasma is accelerated at higher speeds than the average solar wind velocities. The winds are then called fast solar winds.

In the observations, the corona contains three distinct spectra. The first is called K-corona (Kontinuum), it refers to the photospheric light that gets through the corona, also known as "white corona". The second is the F-corona (Frauenhofer), and it refers to the absorption lines of the photons scattered by dust particles. The last one is the E-corona (Emission), and represents the emission lines that the corona produces due to its high temperature (Golub and Pasachoff, 2010).

2.2 Solar magnetic activity

The Sun features a strong magnetic activity that is spread over 11 years cycles, or 22 years if we include magnetic polarities (Newkirk and Frazier, 1982).

At the beginning of the research about the origin of the solar magnetic fields, it was thought that it could come from a primordial magnetic field (Newkirk and Frazier, 1982). This one would have been created at the beginning of the Sun's life, and would have lasted until our days. However, the occurrence of a cycle has denied this theory. Through the calculation of the sunspot number present on the surface of the Sun, an activity cycle of 11 years has been found. This cycle usually starts with 3 years of an increase, followed by a maximum and by a 8 years decrease of the sunspot numbers (Schove, 1983). This discovery led the scientists to elaborate a new theory called the solar dynamo (Ossendrijver, 2003).

The solar tachocline could be a major actor of the solar dynamo (Dikpati, 2006). Indeed, it is known from hydrodynamics that charged and moving particles generate a magnetic field. The convection zone, containing moving ionised or partially ionised matter, amplifies the magnetic field and produces the large scale magnetic field around the Sun. It is important to notice that a magnetic field tends to increase the stability under convection. In fact, such cancellations of the convectivity due to large magnetic fields happen on the surface of the Sun. Those regions cool down and are observable on the photosphere as sunspots. The solar dynamo is the source of several phenomena. Firstly, it is crucial to note that the rotation of the Sun is not homogeneous. A differential rotation is observed on the surface of the Sun. Indeed, the matter is rotating faster at the equator than at the poles. Around the equator, the Sun rotates one time every 25 days. This rotation is called sidereal rotation. Whereas, around the poles, it rotates one time every 35 days (Zell, 2017). On the other side, the matter drags the magnetic field lines. Consequently, the magnetic field lines wrap around the equator during the differential rotation. This effect, illustrated in figure 2.4, is called the ω-effect. In addition, a Coriolis force can kink the magnetic field lines, creating loops, the α-effect (Ossendrijver, 2003). The distortion of those lines determines how active the Sun

is.

Regarding the observation, this solar dynamo manifests, as mentioned, as sunspots. The more numerous and complex the sunspots are, the more active the Sun is. Nonetheless, the sunspots seem to obey some organisational rules. Indeed, a sunspot with a polarity seems to come together with another sunspot of the other polarity. Moreover, this pair of sunspots is composed of a leading and a trailing one. The trailing one follows the leading one with respect to the solar rotation direction. Furthermore, the leading sunspots of each hemisphere always have the same polarity. The polarities of the sunspots on both hemispheres are opposed. After a period of 11 years, the polarity of the hemispheres reverse, implying an overall cycle of 22 years called Hale's cycle. Finally, all sunspot pairs are tilted with respect to the solar equator, with the leading spot closer to this equator. This is known as the Joy's rule. An additional law, called Spörer's law, claims that the sunspots migrate towards the equator with time (Ossendrijver, 2003). A visualisation of the latitude of the sunspots over time is the so-called Butterfly diagram.

While sunspots are mainly associated with close magnetic field lines, coronal holes are associated with open magnetic field lines. These open lines accelerate the plasma in the interstellar medium and create the fast solar wind. The coronal holes, usually located at high latitudes can migrate at lower latitudes during periods of higher solar activity (Cranmer, 2009). Then, the fast solar wind has a greater impact on the Earth as the pressure on the magnetosphere of the Earth increases with the solar wind speed.
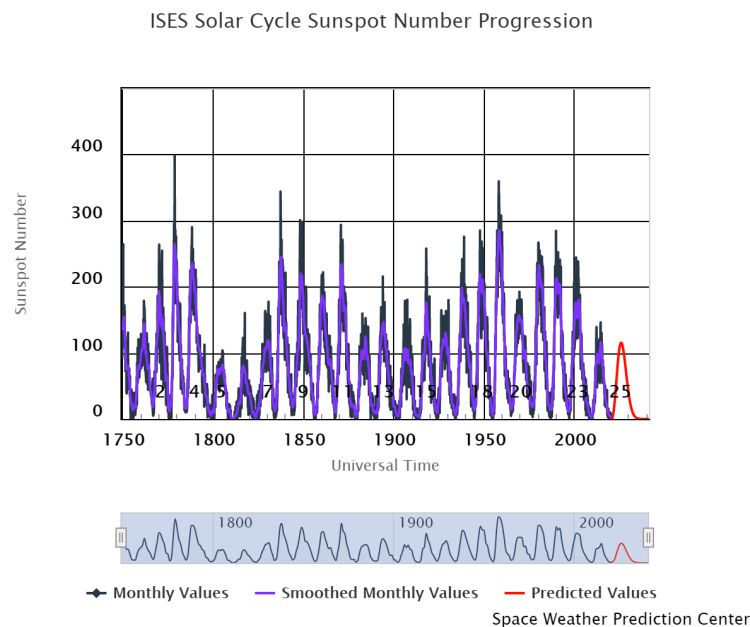
Fig. 2.3: The evolution of the sunspot number since 1750 and the appearance of a solar cycle from the Space Weather Prediction Center https://www.swpc.noaa.gov/products/solar-cycle-progression.

The ω-effect
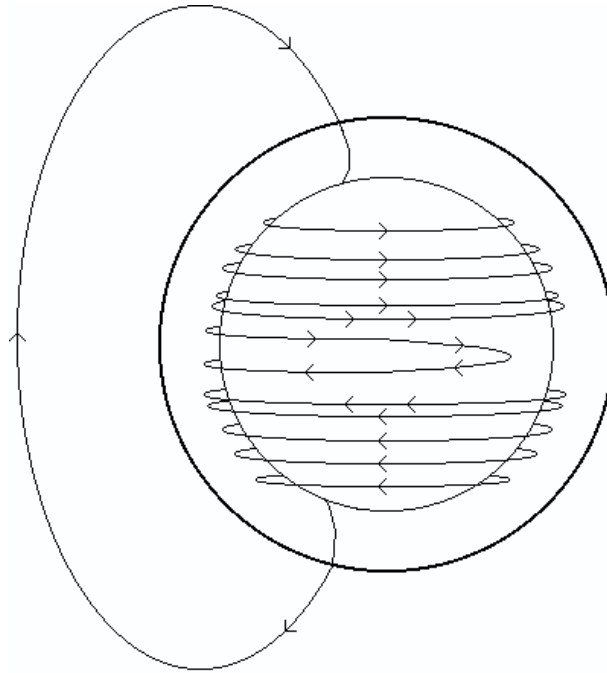
Fig. 2.4: The mengetic field lines wrap around the Sun due to the solar differential rotation. Credits: https://solarscience.msfc.nasa.gov/dynamo.shtml, by Hathaway (2014).

2.3 The Solar wind

The solar wind is a constant flow of particles coming from the Sun that propagates in the interstellar medium.

The transition between the hot and dense corona with the sparse and cool interstellar medium creates a pressure-gradient force that accelerates the plasma away from the Sun. This expansion of the solar corona is called the solar wind.

The plasma of the solar wind can drag the magnetic field lines of the Sun. The solar wind expands in a radial direction, whereas the magnetic field lines' feet, rooted in the Sun, follow the differential rotation. As a result, the magnetic field lines and the solar wind create a spiral structure around the Sun shown in figure 2.5. This spiral is called Parker's spiral (Parker, 1958). The two tails (ion and dust tail) of comets are a proof of the existence of this solar wind. One is a result of the solar radiation pressure, the other is due to the solar wind, tilted with respect to the radial direction Sun-comet.
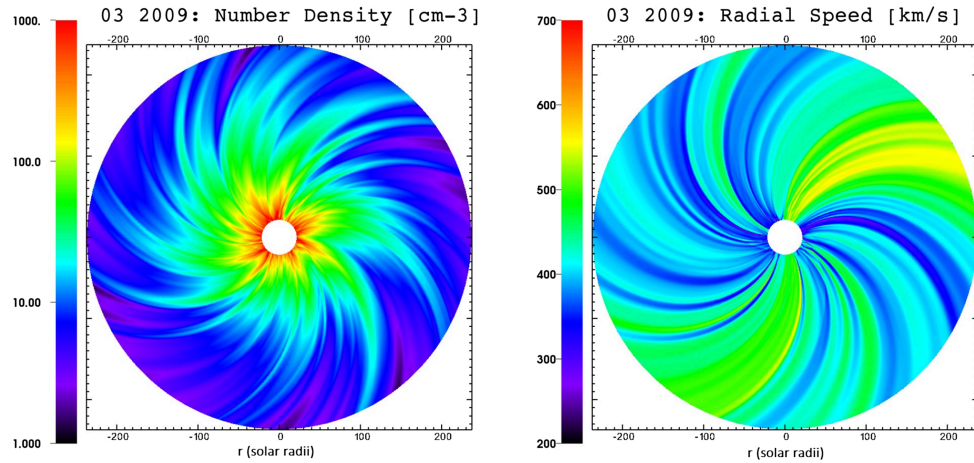
Fig. 2.5: Reconstruction of Parker's spiral. The left panel shows the number density and the right panel the radial velocity. The magnetic field lines follow the same structure. (Biondo1 et al., 2021)
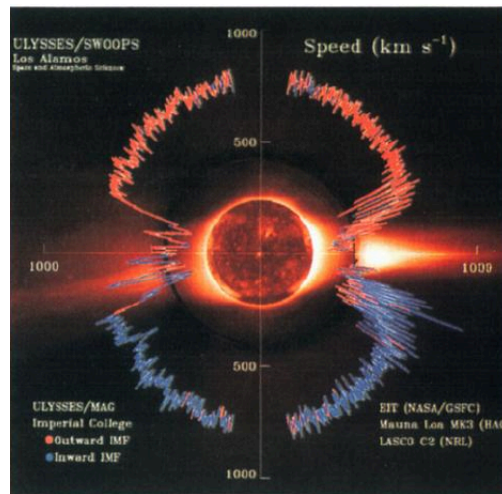
Fig. 2.6: Magnetic polarity as function of heliolatitudes measured by the Ulysses mission with three concentric images taken with the NASA/GSFC E1T instrument (center), the HAO Mauna Loa coronagraph (inner ring), and the NRL LASCO C2 coronagraph (outer ring). Each 1-hour averaged speed measurement has been color coded to indicate the orientation of the observed IMF: red for outward pointing and blue for inward. Digital versions of this figure are available for scientific and educational purposes through the Ulysses/SWOOPS homepage (http://nis-www.lanl.gov/nis- projects/swoops/) by McComas et al. (1998).

In fact, two types of solar winds are observed:
Namely, the slow and the fast solar wind. The slow solar wind emanates from the solar corona expansion in the region where the magnetic field lines are closed. Its velocity is about 400 km s^{-1}.

The fast solar wind is accelerated by the open magnetic field lines of the Sun (Verscharen and B. A. Maruca, 2019). The open magnetic field lines can be found in coronal holes. Figure 2.6 shows the speed of the solar wind with respect to the latitudes, as well as the

Interplanetary Magnetic Field (IMF). In point of fact, the regions where the solar wind is fast, coincide with the regions where the magnetic field lines are open. This figure presents the Sun at its minimum of activity and the coronal holes are situated at the poles i.e. at high latitudes (McComas et al., 2000).

When the fast solar wind catches up the slow solar wind, those two interact. A co-rotating interaction region (CIR) is a region where the fast solar wind interacts with the slow solar wind, creating a pressure gradient (Jian et al., 2009).

As the solar wind expands supersonically outwards, it encounters the interstellar density pressure. A so-called termination shock appears where the solar wind speed becomes subsonic. Beyond the termination shock lies a region of transition called heliosheath. It is the region where the equilibrium between solar wind pressure and interstellar density pressure is reached. At the end of this heliosheath, the heliopause is drawing the end of the heliosphere (Pogorelov et al., 2016). Figure 2.7 is showing two plots of the reconstruction of the heliosphere. The left panel shows the density distribution on the polar plane, and the second one the magnetic field strength on this same plane.
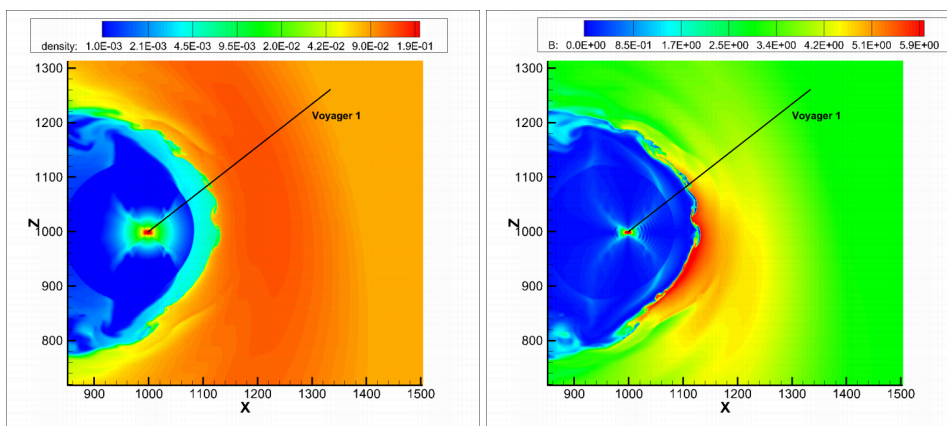
Fig. 2.7: Reconstruction of the termination shock, heliosheath and heliopause. Originally, this reconstruction aimed at showing the instabilities of the heliopause (Pogorelov et al., 2016).

2.4 Coronal Mass Ejection (CME)

The magnetic activity of the Sun gives birth to multiple phenomena on the surface or in the atmosphere of the Sun. One of these phenomena is the Coronal Mass Ejection (CME). In few words, it can be seen as a large eruption of plasma and magnetic field that can drag over 10 billion of tons of matter and often has over 10^{32} erg of energy (Antiochos et al., 1999). In the next sections, we will see what the causes and the characteristics of such CMEs are.

2.4.1 Causes

As we have already seen in the solar magnetic activity section, the solar magnetic field lines kink due to the Coriolis force. In fact, these lines can do much more than just kink. They can twist and shear, and thereby, store energy. The base structure of a CME onset is composed of a core, which is made of several shear magnetic field lines that link regions of opposite polarities, itself covered by some surrounding magnetic field lines (Moore and Sterling, 2006). Often, those phenomena come together with prominences that are accumulations of chromospheric plasma (Taubenschuss, 2009). We can, as an example, illustrate and explain the start of an eruption by ideal magnetohydrodynamic (MHD) instability.
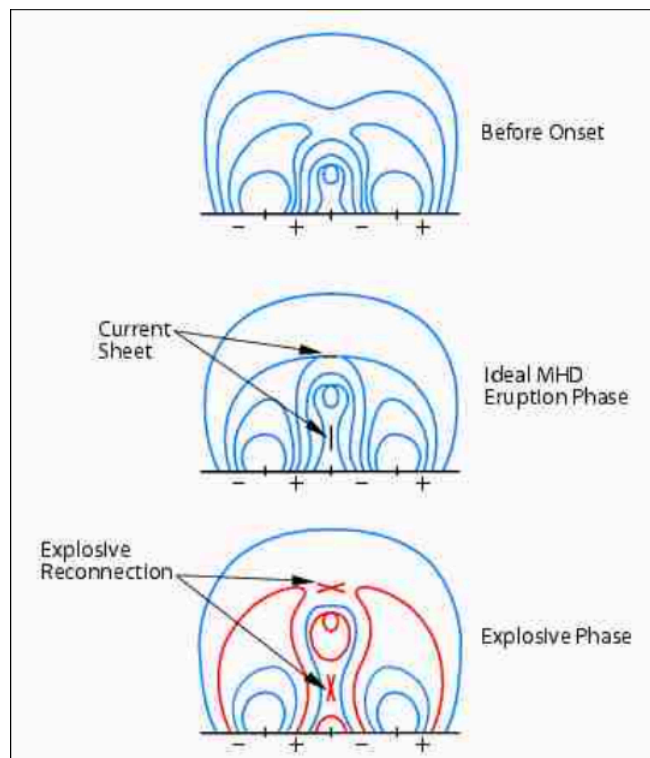
Fig. 2.8: Solar CME onset by the ideal MHD instability followed by magnetic reconnection (non-ideal MHD). The blue lines are the magnetic field lines. The plus and minus under the bases are the polarities of the surface of the Sun. (Moore and Sterling, 2006).

On the figure 2.8, we can see a quadrupolar based CME onset. On the first panel, we can distinguish the core as the central lobe and some surrounding closed magnetic lines. The differences to the second panel are the two current sheets that appear at the null point (the point over the core), and between the legs of the central lobe, under the core. Those current sheets appear when two magnetic field lines of opposite direction get closer to one another. At this point, the magnetic tension is relatively high, meaning that a relevant quantity of energy is stored in the system. Eventually, this equilibrium will cease and

magnetic reconnections will occur. The magnetic field lines will rearrange in order to lower the tension of the structure. Yet, the energy that was stored in the system is released as thermal and kinetic energy, allowing the core to reach high velocities (Moore and Sterling, 2006). Two other possibilities of CME onsets are the internal and external tether-cutting reconnections. Those cases are similar to the Ideal MHD instability, the difference being that the two current sheets and reconnections do not occur simultaniously. The reconnection of the null point happens earlier than the one between the core's legs in the external tether cutting reconnection. Whereas, in the internal tether-cutting reconnection, the magnetic reconfiguration takes place earlier between the legs of the core than at the null point. These three cases of CME initiation are well described and detailed in the article of Moore and Sterling (2016).

Some other initiation models exist and explain how a CME could start. It is the case of toroidal forces in a current loop. This model assumes an arc-like current loop located in the solar corona, whose feet are attached to the solar photosphere. When becoming unstable, i.e. the fluxes below the loop becoming greater than the fluxes above it, the current loop could extend through the background gas, triggering shocks as well as shock heating of the surrounding gas. Interestingly, the trigger of the instability could come from subphotospheric dynamics of the current structure, and thereby, the corona would have no contribution (Chen, 1989).

A CME event evolves through three distinct phases. The first is the onset. The second phase is the acceleration phase. Mainly, the core behaves as if it would not be magnetically connected to the Sun anymore, and therefore, the gradient of the magnetic field line density is accelerating the cloud outwards. Finally, the third phase is the propagation. Once out of reach, the magnetic cloud has enough mass and kinetic energy to propagate through the interstellar medium. Often, the decelerating due to the interstellar medium particle density can be neglected (Zhang and Dere, 2006).

2.4.2 Characteristics

In figure 2.9, we recognize the CME onset mechanism explained by figure 2.8. In addition, a large structure labeled as "Large Coronal Loop" is shown. This feature is what we call the flux rope. In a few words, it is a group of magnetic field lines circling around a common axis. Indeed, it forms a rope connecting two locations of the Sun having opposite polarities. This flux rope is represented as a straight magnetic line in the center, and an additional magnetic line turning around the latter. We will call the center line flux rope center or flux rope axis. Even though flux ropes do not contain only two magnetic field lines, an ideal flux rope indeed contains a flux rope axis at the center with other magnetic field lines turning around it. In fact, the number of times that the field lines are turning around this flux rope

axis is called the twist. The twist of field lines seems to be larger for field lines further away from the flux rope center.

Figure 2.10 is the coronagraph image data of a real CME, visible on the left side of the picture. We can distinguish a bright surrounding loop with a bright core in the middle. These two features are separated by a dark region. This region is called the cavity. The cavity is where the magnetic flux rope is located. The bright front structure is the dense hot plasma pushed by the magnetic flux rope in the interstellar medium. In fact, the fast CME drags the solar wind with it and creates a shock on its front boundary (Reames, 2000; Vršnak and Cliver, 2008).
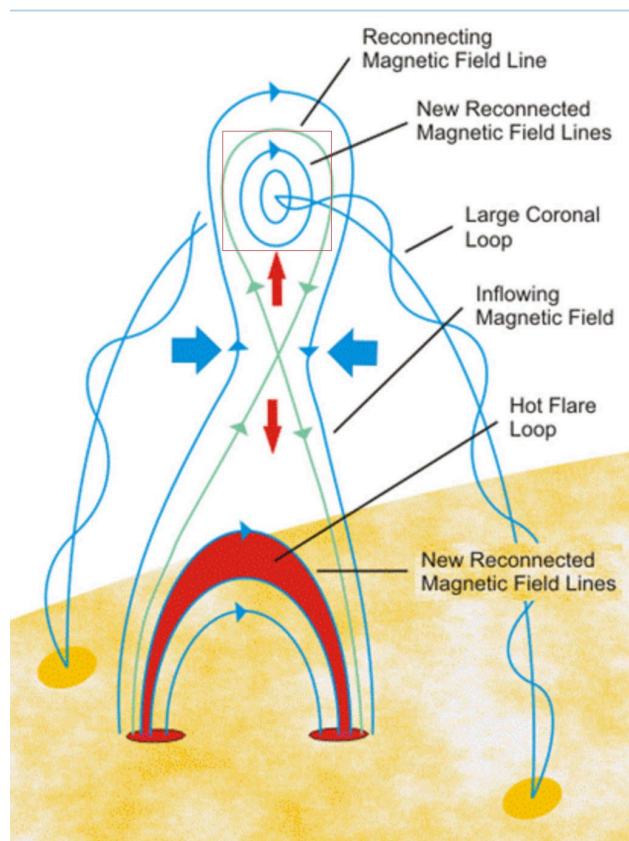
Fig. 2.9: Scheme of a coronal mass ejection onset. The blue solid lines are magnetic field lines. We recognize the ideal MHD eruption described in figure 2.8. The flux rope is labeled a "Large Coronal Loop" and represented with its twist. The red square surrounds a region which is zoomed in in figure 2.11. Credits: http://www.earthquakepredict.com/2017/07/what-is-coronal-mass-ejection-cme.html

The reason why the cavity appears dark is that plasma density and temperature are low in this region. As a result, the gas pressure $P_{gas} = nkT$ drops (n and T are the density and the temperature respectively). However, the pressure balance is such that the magnetic pressure $P_{mag} = \frac{B^2}{2\mu_0}$ is high in this region. The β parameter, $\beta = \frac{P_{gas}}{P_{mag}}$, is a useful indicator for describing the different regions. Indeed, if the magnetic field has the priority over the

plasma, β will drop below one, as in the cavity or flux rope. This means that the magnetic field lines dictate how the plasma moves, and the plasma is frozen-in. If the β parameter is over one, this means that the plasma has the priority over the magnetic field. In this case, the plasma drags the magnetic field lines with it (Nieves-Chinchilla et al., 2016). The CMEs have speeds that range from 100 km s^{-1} to over 1200 km s^{-1}, with some approaching 3000 km s^{-1} (NOAA, 2020; Gosling et al., 1976).
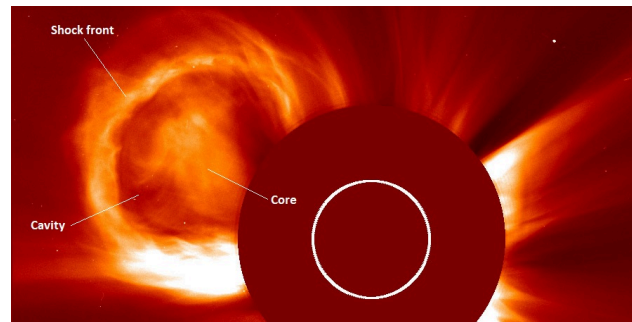
Fig. 2.10: SOHO/LASCO coronograph image of the event on the 10th of February 2015, at 12:44 UTC. The bright features are the hot and dense plasma, while the dark region in between is the magnetic flux rope.

Symmetries are important in the Grad-Shafranov reconstruction, as those can be associated to conserved parameters. Ideal CMEs contain some symmetries.
In the ideal case, the toroidal flux in the flux rope is conserved. This means that the number of magnetic field lines connected to the two feet of opposite polarity of the flux rope does not change. In turn, this also means that the magnetic field lines in the flux rope did not reconnect and are, therefore, attached to the Sun.
The expansion of the CME in the interstellar medium respects the self-similar expansion. This means that all the proportions associated with the structure of the CME are conserved over its propagation. As the size of the magnetic cloud increases, the radius of the flux rope increases at the same rate. This phenomenon explains that the plasma velocity decreases linearly inside the flux rope. Indeed, when the spacecraft enters the flux rope, it measures a plasma speed equal to the sum of the mean cloud velocity and the expansion speed. When the spacecraft reaches the center of the flux rope, it measures only the cloud mean velocity as the expansion of the flux rope radius scales with the distance to its center. Finally, when the spacecraft exits the flux rope, it measures a plasma speed equal to the mean cloud velocity minus the expansion velocity.
Another symmetry is represented in figure 2.11. The top panel is the reconstruction of a cross-section of an artificial ideal flux rope with a noise level of 0.01. The green solid line is the path of the spacecraft in the flux rope, and the green arrows are the measurements of the magnetic field in the normal (n) and radial (r) directions (in the plane of the flux rope cross section). The bottom panel shows the measurements of the magnetic field components associated with the spacecraft's path in the cross section. The two panels are displayed such

that the measurements are aligned vertically with the position where the measurements were taken.

The tangential (t) component on the bottom panel is not trivial to connect to the top panel. However, the values of the normal component seem to match the length of the green arrows of the top panel along the spacecraft's path. This feature is called the rotation. When a spacecraft crosses a flux rope, a frame should exist in which this rotation is observable.

In fact, the black solid lines of the top panel are isocontours of RB_ϕ (radial distance times the magnetic field strength in the plane of the cross-section). We see that the structure of those lines constructs closed contours around the apparent center of the flux rope. As these lines are isocontours, it is understandable that the measurements of the magnetic field on these lines have to be related. Hence, a symmetry appears between the path of the spacecraft moving towards the center of the flux rope and its path moving away from the center. On the other side, the measurements are positive on one side and negative on the other. It gives the impression that the magnetic field is rotating around the central axis.

Last but not least, the Grad-Shafranov equation assumes a force-free magnetic field and a vanishing Lorentz force. This has the effect of cancelling the coupling of the electromagnetic force with the other forces. Moreover, the Grad-Shafranov reconstruction makes the calculations in the de Hoffman-Teller frame. This frame ensures that the electric field vanishes (Chao et al., 2014). In addition, this leads to a constant electromagnetic potential four-vector.
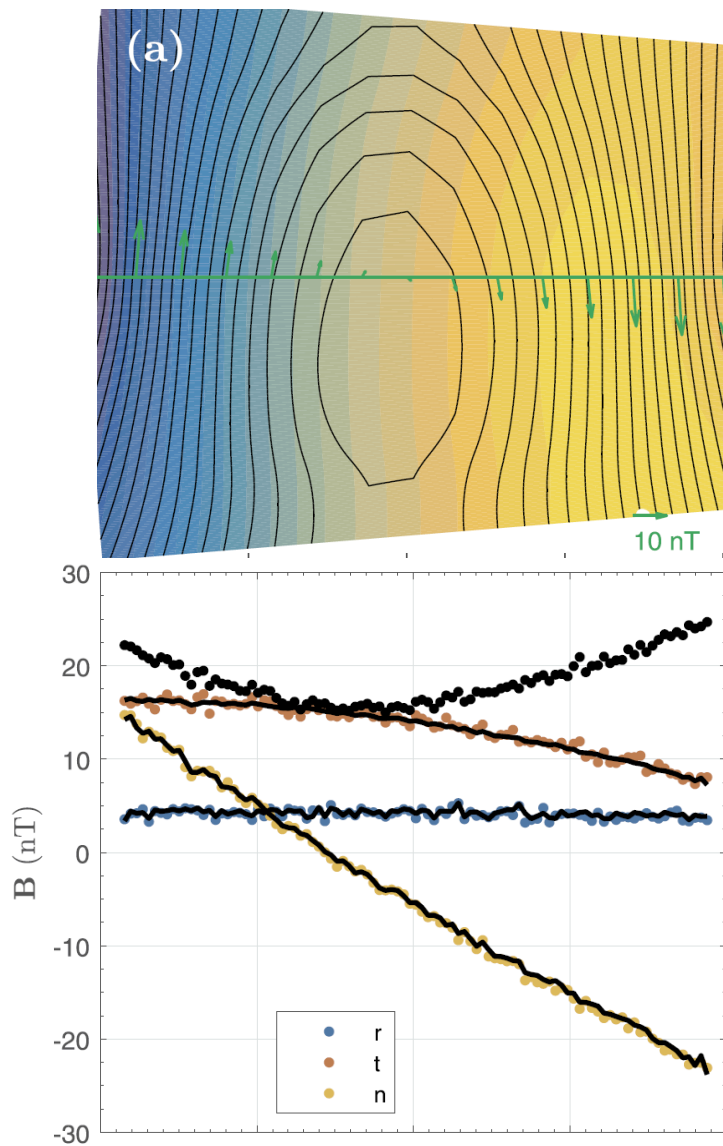
Fig. 2.11: Top panel: Grad-Shafranov reconstruction of the cross section of an artificial ideal flux rope with a noise level of 0.01. The colors map the magnetic field in the transverse direction and can be ignored for the moment. The green solid line is the path of the spacecraft in the flux rope. The green arrows are the measurements of the normal component of the magnetic fields. Bottom panel: Magnetic field components measurement from a spacecraft crossing the flux rope of the panel above. The labels 'r', 't' and 'n' stand for 'radial', 'tangential' and 'normal', respectively. (Hu, 2017).

2.5 The effects on the Earth

The solar wind arrives as a continuous flow of particles at Earth. Whereas CMEs are punctual and have more important consequences on Earth, like magnetic storms.

The Earth possesses a quasi-dipolar magnetic field almost aligned with its rotation axis. However, since the first measurements in 1831, the north magnetic pole of the Earth has wandered in the direction of Siberia, and has even accelerated between 1990 and 2005 (Livermore et al., 2020). The fact remains that the Earth's magnetic field is acting like a shield against heliospheric magnetic fields and charged particles. Much as the heliosphere reaches an equilibrium with the interstellar pressure density at the heliopause, the magnetic pressure of the Earth and the one coming from the Sun are finding a balance point called the magnetopause. The solar winds and CMEs, representing a consequent part of the pressure applied on this shield, are shaping the magnetosphere. Indeed, the incoming pressure on the day side of the Earth is significantly larger than the pressure on its night side. The width of the magnetosphere on the day side reaches about 10 R_E (Earth radius), whereas the mean distance of the magnetopause lies at 30 R_E on its night side (Pulkkinen, 2007). Yet, the magnetotail stretches in the night side direction over hundreds of R_E. Under strong solar wind conditions, the magnetopause can get closer than 6.6 R_E on the day side, having substantial influences on geostationary satellites (Pulkkinen, 2007). While the corotating interaction region (interaction between fast and slow solar winds) has been found to be only moderately geomagnetically effective, some solar flares can accelerate particles that heat the upper atmosphere and have an influence on the drag of low orbit satellites, or even destroy some of their onboard instrumentation. In some cases, those high energetic particles can also change the composition of the atmosphere and damage, with it, the ozone layer (Pulkkinen, 2007). Moreover, the apparition of aurorae around the poles is the result of particles entering the lower atmosphere and ionising the local molecules (Pulkkinen, 2007).

For those who are not simply interested in the Sun and its mysteries, the geoeffectiveness of the space weather itself is a sufficient reason to study it, considering the impacts that it can have on humanity. For example, the solar storm of May 1921 burned out telephone stations and numerous electrical components (Silverman and Cliver, 2001).

The theory of the Grad-Shafranov reconstruction

<div style="text-align: right; font-size: 3em;">3</div>

The Grad-Shafranov method is a symmetry based reconstruction assuming that the magnetic flux rope has a toroidal structure. After explaining the geometry in which we work, I will present the Grad-Shafranov equation. I will describe the reconstruction procedure and then, to illustrate the theory, reconstruct a magnetic cloud.

3.1 Geometry and procedure

At first, the geometry of the reconstruction is going to be presented. Secondly, we are going to explain the Grad-Shafranov equation and its implications for the reconstruction. Finally, we are going to review the procedure of the Grad-Shafranov reconstruction.

3.1.1 The coordinate systems and parameters

The Grad-Shafranov reconstruction assumes that the flux rope has a toroidal structure. Figure 3.1 illustrates two coordinate systems. The global coordinate system is going to be (R,ϕ,Z), and refers to the geometry of the torus. R is the distance from the center of the torus to the center of the flux rope, ϕ is the angle of rotation of the torus, and Z is, therefore, the symmetry axis of this torus.

On the other side, the local coordinate system is also a cylindrical coordinate system: The one of the flux rope itself. Locally, the flux rope can be approximated to a straight cylinder with coordinates (r,θ,z). r is the distance to the flux rope's center, z assimilates with the flux rope axis, and θ is the third normal component of this base.

In the reconstruction, we will be interested in the parameters describing the geometry of the torus:

R_0 is the major radius of the torus. It is the distance between the center of the torus and the center of the flux rope.

θ **and** ϕ are the orientation angle of the Z-axis. The Z-axis is perpendicular to the plane of the torus. The orientation of the Z-axis in the solar ecliptic yields, therefore, the orientation of the torus with respect to the ecliptic plane. Note that these angles have

nothing to do with the variables of the global coordinate system decribed in figure 3.1, even though their names are the same.

r_0 is the radius of the flux rope. It is the distance between the center of the flux rope and its outer boundary.

b is the impact parameter. It is the point of closest approach of the spacecraft to the center of the flux rope.
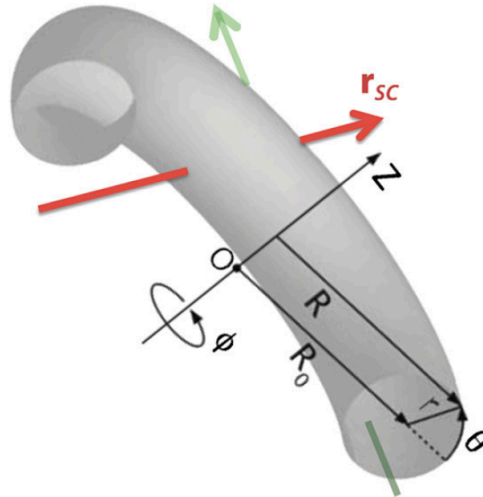
Fig. 3.1: Geometric visualisation of the toroidal flux rope and the parameters describing it, i.e., the Z-axis origin and orientation, the major radius R_0, the invariant direction ϕ and the local variables of the cross section (r,θ) (Hu, 2017).

3.1.2 Calculate R_0 with the self-similar expansion

It is already possible to calculate the main radius of the flux rope R_0. Under the assumptions that self-similar expansion takes place and that the spacecraft crosses the center of the flux rope ($b = 0$), we can deduce the major radius R_0 from the plasma velocity.

In the figure 3.2, we see the frame in which the calulations can be made. $|\vec{r_a}|$ is the distance from the Sun to the center of the flux rope. $|\vec{r_1}|$ and $|\vec{r_2}|$ are respectively the distances from the Sun to the enter and the exit points of the spacecraft in the flux rope. For an ideal flux rope, we derive:

$$r_a = 2R_0 + \bar{v}t \qquad\qquad r_1 = 2R_0 - r_0 + \bar{v}t - et \qquad (3.1)$$

$$r_2 = 2R_0 + r_0 + \bar{v}t + et \qquad\qquad r_{sc} = 2R_0 + r_0 \qquad (3.2)$$

$$d(t) = |r_2 - r_a| = r_0 + et \qquad\qquad D(t) = \frac{r_a}{2} = R_0 + \frac{\bar{v}t}{2} \qquad (3.3)$$

Where $\bar{v}$ is the mean velocity of the cloud, R_0 is the major radius at $t = 0$, r_0 is the flux rope radius at $t = 0$ and e is the expansion speed of the flux rope's boundary. $r_{a,1,2,sc}$ are the distances from the Sun to the respective points of the figure 3.2. $D(t)$ and $d(t)$ are the time dependant major radius and flux rope radius.

The time of entry of the spacecraft in the flux rope is $t = 0$. $\bar{v}$ is the mean velocity of the cloud and e is the velocity of the boundary of the flux rope with respect to its center i.e., the expansion velocity. $D(t)$ and $d(t)$ are the radii of the torus and of the flux rope respectively. By solving $r_1 = r_{sc}$ for t, we find the time of exit of the spacecraft $t^\star = \frac{2r_0}{\bar{v}-e}$. We can compute the radii at $t = 0$ and $t = t^\star$:

$$d(t = 0) = r_0 \qquad\qquad d(t^\star) = r_0 + \frac{2r_0 e}{\bar{v} - e} \qquad\qquad (3.4)$$

$$D(t = 0) = R_0 \qquad\qquad D(t^\star) = R_0 + \frac{2\bar{v}r_0}{2(\bar{v} - e)} \qquad\qquad (3.5)$$

The self-similar expansion means that $\frac{d(t=0)}{D(t=0)} = \frac{d(t^\star)}{D(t^\star)}$. Solving this equation for R_0 gives us $R_0 = \frac{\bar{v}r_0}{2e}$. In figure 3.5, we note a velocity decrease from 800 km s^{-1} to 600 km s^{-1}. We can make a quick calculation by taking $\bar{v}$ as 700 km s^{-1} and e as 100 km s^{-1}. From figure 3.12, we have the r_0 for the same cloud. It is approximately 0.2 AU in this case. We use our solution and obtain a R_0 of 0.7 AU.
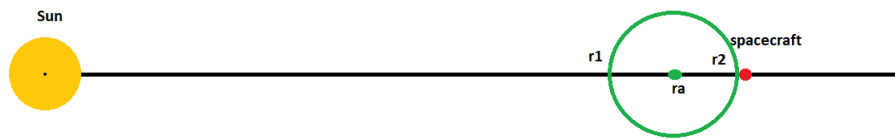
Fig. 3.2: Sketch of the system Sun-spacecraft-flux-rope. The yellow dot is the Sun, the green circle is the outer boundary of the flux rope and the red dot is the position of the spacecraft. The points r1, ra and r2 are the rear boundary, the center of the flux rope and the front boundary, respectively.

3.1.3 The Grad-Shafranov equation

The Grad-Shafranov equation has been found in 1958 from a series of hypotheses (Grad and Rubin, 1958). The first hypothesis is to suppose an invariant axis, such as $\frac{\partial}{\partial z} = \frac{\partial}{\partial \phi} = 0$, constraining $B = \nabla \times A$. Additionally, we also assume balance between the magnetic forces and the pressure on the isosurfaces of the structure (here, a torus), which implies $\nabla p = j \times B$. Furthermore, it has to respect the two Maxwell equations: $\nabla \times B = \mu_0 J$ and $\nabla \cdot B = 0$. After some manipulations detailed by Haverkort (2009), it is possible to derive the Grad-Shafranov equation:

$$R \frac{\partial}{\partial R} \left(\frac{1}{R} \frac{\partial \Psi}{\partial R} \right) + \frac{\partial^2 \Psi}{\partial Z^2} = -\mu_0 R^2 \frac{dp}{d\Psi} - F \frac{dF}{d\Psi} \tag{3.6}$$

This equation can also be written as:

$$\nabla^2 A = -\mu_0 \frac{d}{dA} \left(p + \frac{B_z^2}{2\mu_0} \right). \tag{3.7}$$

From equation 3.7, we can rewrite the Grad-Shafranov equation in a (r, Θ) coordinate system as:

$$\frac{1}{r} \frac{\partial}{\partial r} \left(r \frac{\partial \Psi}{\partial r} \right) + \frac{1}{r^2} \frac{\partial^2 \Psi}{\partial \Theta^2} - \frac{1}{R} \left(\cos \Theta \frac{\partial \Psi}{\partial r} - \frac{\sin \Theta}{r} \frac{\partial \Psi}{\partial \Theta} \right) = -\mu_0 R^2 \frac{dp}{d\Psi} - F \frac{dF}{d\Psi} \tag{3.8}$$

The three equations are equivalent. Equation 3.6 is the toroidal version of equation 3.7 and the two variables F and Ψ are defined as:

$$F = \frac{RB_\phi}{\mu_0} \tag{3.9}$$

$$\Psi = RA_\phi \tag{3.10}$$

There is no analytical solution to this equation. However, we request Ψ to be single valued, meaning that the source function A_ϕ should only take one value for each R. Besides, the formulation of equation 3.8 limits the geometry parameters to a Z-axis orientation and a major radius R_0. Since the spacecraft position is fixed and known (it is located at the Lagrange point L1), the major radius parameter can be replaced by the origin of the Z-axis. Along with the radius of the flux rope, every geometrical parameter has been introduced.

3.1.4 Determination of the Z-axis orientation

The first step of the reconstruction is to determine the Z-axis orientation. The code minimises the residues of a function that is evaluating the symmetry of the flux rope. That means that the code is maximizing the symmetry.

In the global coordinate system (R,ϕ,Z), a cross section is defined as a slice of the torus perpendicular to the e_ϕ base vector. As illustrated in figure 3.1, the path of the spacecraft may cross several of these cross sections. In other word, $\overrightarrow{r_{sc}} \cdot \overrightarrow{e_\phi} \neq 0$. Hence, it can be laborious to rebuild the symmetry of a single flux rope cross section. With the condition $\frac{\partial}{\partial \phi} = 0$, we can project every crossed cross-sections on one of them along the $\overrightarrow{e_\phi}$ base vector. Note here the importance of the projection under rotation " along the $\overrightarrow{e_\phi}$ base vector ", as it is a symmetry under rotation. Indeed, a usual Cartesian projection could give wrong results. To truly understand how the code works, we have to look closer at how a cross section is constructed, and which symmetries we are looking for within it.
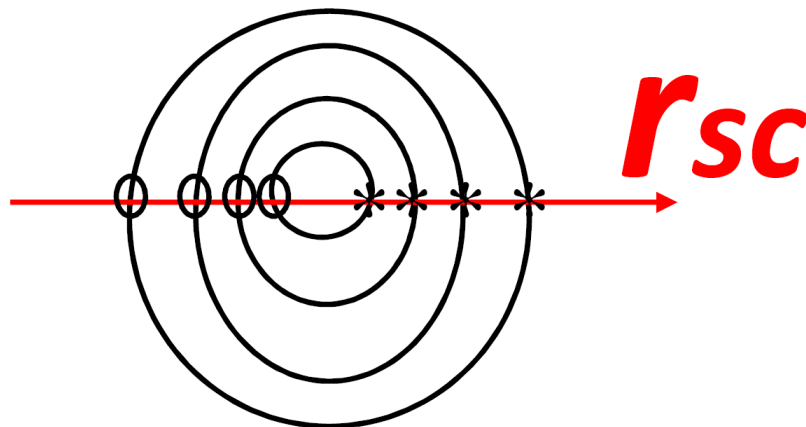
Fig. 3.3: Magnetic flux rope cross section with isolines of constant $F(\Psi)$ (solid lines). The smaller circles represent the inbound measurements and the stars the outbound ones. r_{sc} is the path of the spacecraft. (Hu, 2016).

Figure 3.3 shows the two branches of the spacecraft's path inside the flux rope. Namely, the inbound and the outbound branches. The symmetry that we were searching for is a symmetry between those two branches. In fact, we are searching to minimise the differences between the values of F on the inbound and outbound branches. Indeed, the contours in figure 3.3 are isocontours. The measurements of F on the inwards path should, therefore, have their twin measurements on the outwards path. In reality, we are going to measure the

differences between the measurements of F on the inwards and outwards branches. This is calculated as a residue function that takes the following form:

$$Res = \frac{[\sum_i (F_i^{inbound} - F_i^{outbound})^2]^{\frac{1}{2}}}{|\triangle F|}$$

(3.11)

where $\triangle F = F_{max} - F_{min}$.

We know how to project the measurements on one cross-section of the torus, and we know how to compute a minimal residue, that evaluates how symmetric the flux rope is. Yet, this is not quite enough to reconstruct magnetic clouds. We do not know how to project our measurements, since we do not know in which direction the e_ϕ base vector points. Moreover, we have only one residue that tells us how symmetric the flux rope is, but no other residues to compare it with. We need to introduce the Z-axis orientation, Z-axis origin and the radius of the flux rope r_0.

First, the flux rope radius is the easiest to compute as it is fixed by the chosen boundaries of the cloud, the impact parameter derived from the reconstruction and the cloud velocity. Secondly, the origin of the Z-axis can be seen as the point where the Z-axis crosses the ecliptic plane. On this same plane, a polar grid of radius 1 AU is constructed. Each knot of this grid is at the origin of the second step. An example of this grid is given in the figure 3.9. This second step consists of building, over each knot of the equatorial grid, a unit one half-sphere. The vector from the center of this half-sphere to one of the half-sphere surface's point stands for a direction i.e. a Z-axis orientation. Therefore, similarly to step one, the code is constructing a grid on the surface of this half-sphere, and testing all the possible directions for the Z-axis orientation. Figure 3.7 shows a visualisation of one of these half-spheres. To summarize, each knot on the half-sphere, standing for one Z-axis orientation, is going to yield one residue, and each knot on the equatorial plane's grid is yielding a half-sphere. The code is hence testing every Z-axis orientation at every point of the equatorial plane. The computed residues can be compared. The lowest of the residues gives the most symmetric flux rope as well as the Z-axis orientation and origin creating it.

3.1.5 Determination of the Z-axis origin

The second step is mainly a re-run of the first step with an additional comparison with the measured magnetic field components. Two variables are added. They release understandable information about the goodness of the reconstruction.

This second step does not re-run the orientation of the Z-axis. The Z-axis orientation is hence fixed by the previous computation. Whereas, the Z-axis origin is going to be

recalculated with the additional varibles χ^2 and Q. χ is called the goodness-of-fit, as it is an evaluation of the differences between the measured magnetic field and the reconstructed one. Q is the probability of the associated χ^2 having the lowest value possible. Explicitly:

$$\chi^2 = \frac{1}{N} \sum_{i=X,Y,Z} \sum_{j=1}^{N} \frac{(b_{ij} - B_{ij})^2}{\sigma_{ij}^2} \tag{3.12}$$

$$Q = 1 - chi2cdf(\chi^2, dof) \tag{3.13}$$

In these equations, b describes the computed magnetic field, B, the measured magnetic field, σ the uncertainties given by CDAWeb, dof, the degrees of freedom of the system and $chi2cdf$, a cumulative distribution function of χ^2.

We notice, from equation 3.12, that if the differences between measured and reconstructed magnetic fields are lower than the uncertainties, their ratio is going to be inferior to one. Naturally, through the summation, we obtain N terms like these. Dividing by N gives the averaged relation between differences in magnetic fields and uncertainties. Summing over the three Cartesian components makes us think that, theoretically, a χ^2 inferior to three is a successful reconstruction. In fact, χ^2 has to be inferior to two to consider the reconstruction as a success (Hu, 2017). From equation 3.13, we can summarize the function $chi2cdf$ by being the probability of χ^2 having a lower (i.e., a better) value. Thus, Q represents the probability of the fit (and the χ^2) being the best possible outcome. In a few words, χ should be below two and Q should be high for a successful reconstruction.

3.1.6 Reconstruction and Parameters

By solving the Grad-Shafranov (GS) equation, the code is able to reconstruct the cross section of the flux rope and yields important information about the cloud. For example, the code calculates the maximum magnetic field in the z direction, the poloidal and toroidal fluxes, the major radius R_0 and the impact parameter b.

To understand what poloidal and toroidal fluxes represent, we can imagine our torus in cylindrical coordinates (see figure 3.4). The toroidal flux is the magnetic flux (the sum of the magnetic field lines) crossing through one of the cross sections in the plane (R,Z). Equivalently, it is the flux in the z direction of the local coordinate system. The poloidal flux is then the magnetic flux crossing the surface parametrized by: $R \le R_0$, $\phi \in [0, 2\pi]$ and $Z = 0$. Those values are directly linked to another value called twist.

The twist is the number of loops that a magnetic line completes over a certain distance. Here, the magnetic lines are turning around the flux rope's center. The twist is then used to describe how often those lines are circling around this axis (see figure 3.13).

Now, to highlight the link between twist, poloidal flux and toroidal flux, we will have to

make the projection of the magnetic field lines on the local base (r, θ, z). We are going to assume that each line stays at a fixed distance of the flux rope's center. We will also assume that the twist does not change over the line. Hence, the lines are turning on the surface of a cylinder of radius r_0 and evolve always at the same pace. The projection of the magnetic field lines (call it $\vec{B_l}$) is made with the components $\vec{e_\theta}$ and $\vec{e_z}$.

Now, if $\vec{B_l} \cdot \vec{e_\theta} = 0$, it means that the magnetic field lines are parallel to the flux rope axis z, and therefore, that the twist vanishes. Equally, this means that the magnetic field lines are perpendicular to the surface (r, θ), hence, only creating a toroidal flux.

On the other hand, if $\vec{B_l} \cdot \vec{e_z} = 0$, this means that the magnetic field line has no motion in the direction of the flux rope axis. This is, the magnetic field line stays in the (r, θ) plane. The flux is then only poloidal, and the twist infinite.

Note that the poloidal flux can be seen as the sum of two fluxes: The flux through the surface of S outside of the flux rope and the flux through the surface of S inside the flux rope (see figure 3.4). We could think that, with a flux rope radius small enough, the contribution of the twist inside the flux rope is going to be a negligible part of the poloidal flux. In fact, in our case, only the flux through the surface inside the flux rope is considered. It is the surface outside that is neglected. It is possible to do so, as outside of the flux rope $\beta > 1$. Hence, the plasma dictates the magnetic field lines how to bend and the magnetic field has no structure. Overall, the magnetic field lines are crossing this surface in both directions and the flux vanishes.
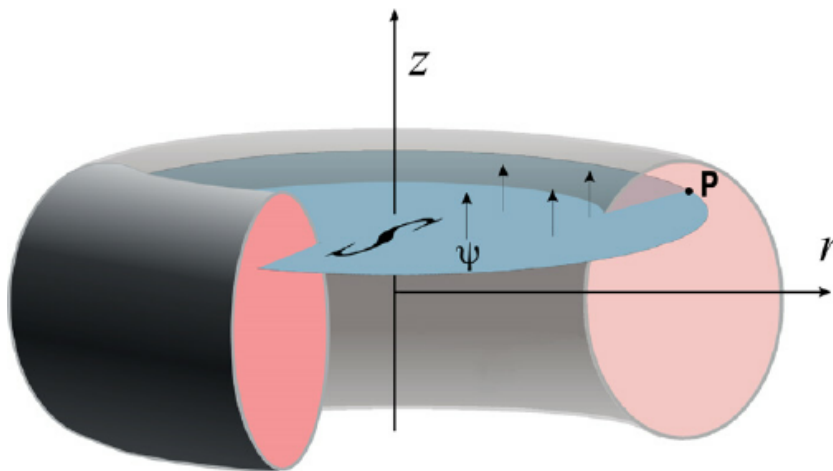
Fig. 3.4: The poloidal and toroidal magnetic fluxes are the sum of the magnetic lines crossing the blue and the pink surfaces respectively. The point P indicates where the center of the flux rope is located on the (r, θ) plane. In the case of the Grad-Shafranov reconstruction, the plane S should be at the hight Z=0. (Yongsheng and Chao, 2008).

3.2 WIND Event on 2004-11-09

The Grad-Shafranov reconstruction that we are testing is based on the new code of Hu (2017). The method is the one developed by Hu and Sunnuerup, originally designed to understand the interaction between the solar wind and the Earth magnetic field (Möstl et al., 2009). In a scientific purpose, it is sensible to test our code, and compare the results with some reliable sources. In fact, this section is either an explanation of the reconstruction method and a proof of the code's efficiency, as it agrees with the results of Isavnin et al. (2011).

3.2.1 The Data

The understanding of the data is required to choose wisely the boundaries of the flux rope. The characteristics of flux ropes have already been explained. The presence or not of these characteristics guide our choice of the boundary selection.

The data of the WIND spacecraft are extracted from CDAWeb. From this source, the data reduction has already been made.

The top plot of the figure 3.5 presents different curves. From the top to the bottom, they are: The total magnetic field and its components, the total velocity of the cloud, the electron temperature, the density, the gas pressure, the magnetic pressure, followed by the proton temperature and the β parameter. On the same plot, colored regions are giving the important parts of the CME. On the left side of the red zone, the data can be understood as the background noise. The red zone, however, contains spikes in almost every component. The magnetic field strongly increases and the plasma speed starts to linearly evolve. On the other hand, the density, the temperature and therefore, the gas pressure all abruptly enhance. This region is the shock-sheath region.

After the shock, the flux rope is dominating. The choice of the flux rope boundaries is a meticulous task and it influences the reconstruction. Inside the flux rope, the magnetic pressure has to overcome the gas pressure. Otherwise, the charged particles would drag the magnetic field lines and dictate its shape to the line's arrangement. Hence, the plasma has to be frozen-in and $\beta < 1$, as highlighted in green in the top panel of figure 3.5.
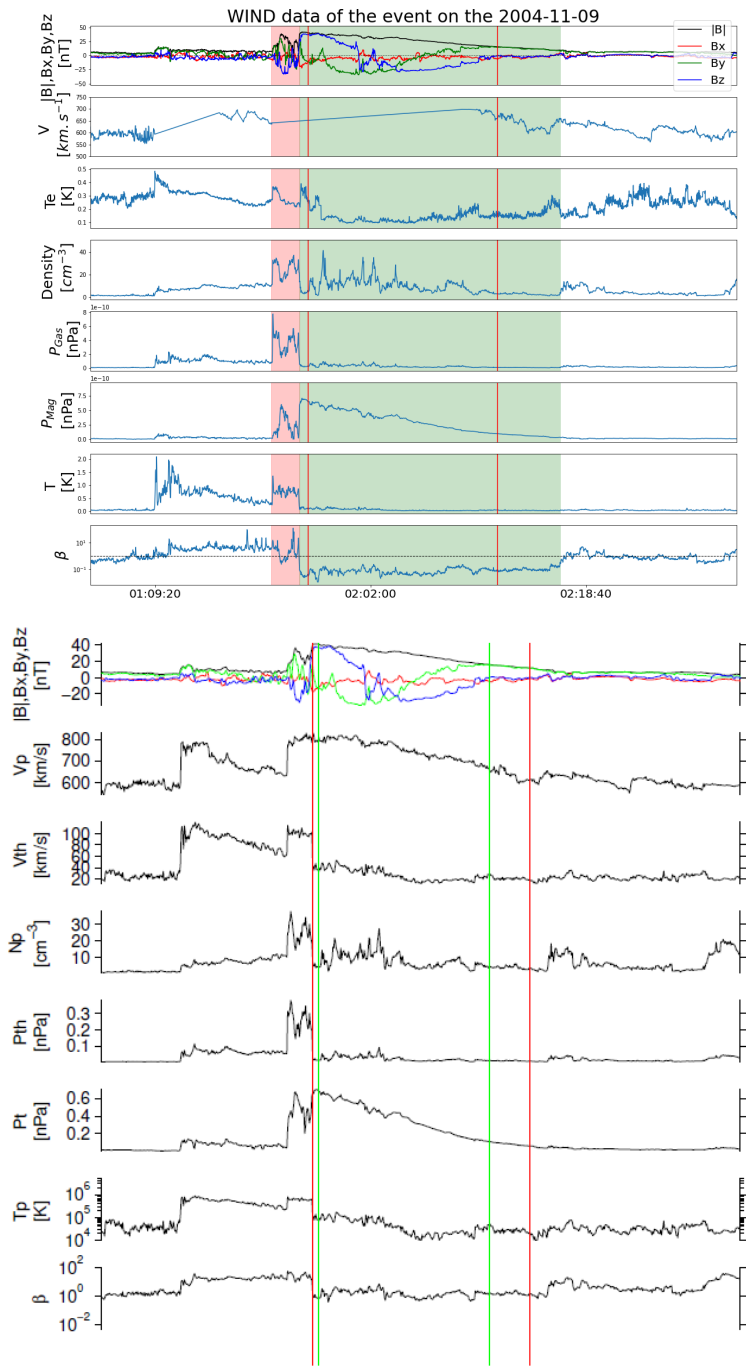
Fig. 3.5: Top: WIND data of the event on 2004-11-09. The red vertical lines are the boundaries taken for the example reconstruction. The red region highlights the data representing the shock. The green region represents the flux rope. Inside this one, $\beta < 1$. The time on the x-axis has the format days:hours:minutes, where 00:00:00 is the beginning of the day 2004-11-08. Bottom: Data used in the article of Isavnin et al. (2011). The green and red vertical lines are the two sets of boundaries used for their reconstructions.

Inside the flux rope, the magnetic field has to be enhanced and relatively smooth. We should also distinguish the magnetic field rotation. Here, the B_z component of the magnetic

field is indeed rotating. As we can see, it drops over time from 30 nT to -20 nT, while the B_x component is stable around 0 nT. However, it happens that the rotation is not easy to recognize. In this case, it is helpful to look at the velocity graph. This one linearly decreases through the flux rope.

To exhibit the rotation of the magnetic field components, we can look at the hodograms of figure 3.6. B_1, B_2 and B_3 are the projections of the magnetic field onto the minimum, intermediate and maximum variance directions, respectively. With λ_1, λ_2, λ_3 their respective eigenvalues. In other words, B_1 is taken to vary the less and B_3 to vary the most. Therefore, the ratio of their eigenvalues should be high (right panel of figure 3.6). B_2 varying at an intermediate speed, the ratio of λ_1 over λ_2 should be significantly lower than the ratio of λ_1 over λ_3.

On the other hand, the hodograms give useful information about the boundaries. Indeed, those plots translate the rotation of the magnetic field into a visual representation. If an anomaly is present on one of the hodograms, it may mean that a part of the data does not belong to the flux rope.
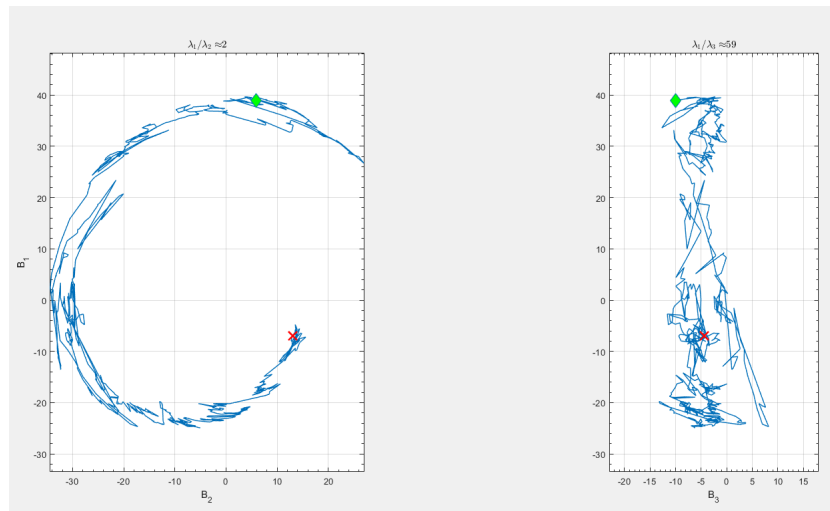
Fig. 3.6: Hodograms displaying B_1 with respect to B_2 and B_3, the projections of the magnetic field in the minimum, intermediate and maximum variance directions, respectively. The left panel translates the rotation of the magnetic field, and the right panel shows the invariant axis.

3.2.2 Finding the orientation of the Z-axis

The reconstruction starts with a first trial-and-error test on the orientation of the Z-axis. As we have already the boundaries from Isavnin's article, we can immediately start running the code and show the first results. The figure 3.7 is the residue map of the Z-axis orientation. It is the main result of the first step of the reconstruction. The blue cross is the point that we consider as a possible Z-axis orientation. In fact, this cross is picked up by hand. A

discussion on the influence of the manual pick is provided in a section 4.5. The residue map is supposed to show an island or a group of islands. The best Z-axis orientation is theoretically selected in the middle of the island, or in the middle of the group of islands. This explains the position of the blue cross. The position of the cross indicates the following angles: $\theta \approx -20$ and $\phi \approx 45$. In fact, these angles are not exactly the angles to compare with Isavnin's ones. Indeed, one of the components is missing in this graph, and the code is giving the three components in Cartesian coordinates. Hence, in order to get the two Z-axis orientation angles, we should transform the three Cartesian coordinates in the three sphercial coordinates following the usual coordinate system transformation's relations:

$$\theta = arctan(\frac{\sqrt{x^2 + y^2}}{z}) \tag{3.14}$$

$$\phi = arctan(\frac{y}{x}) \tag{3.15}$$
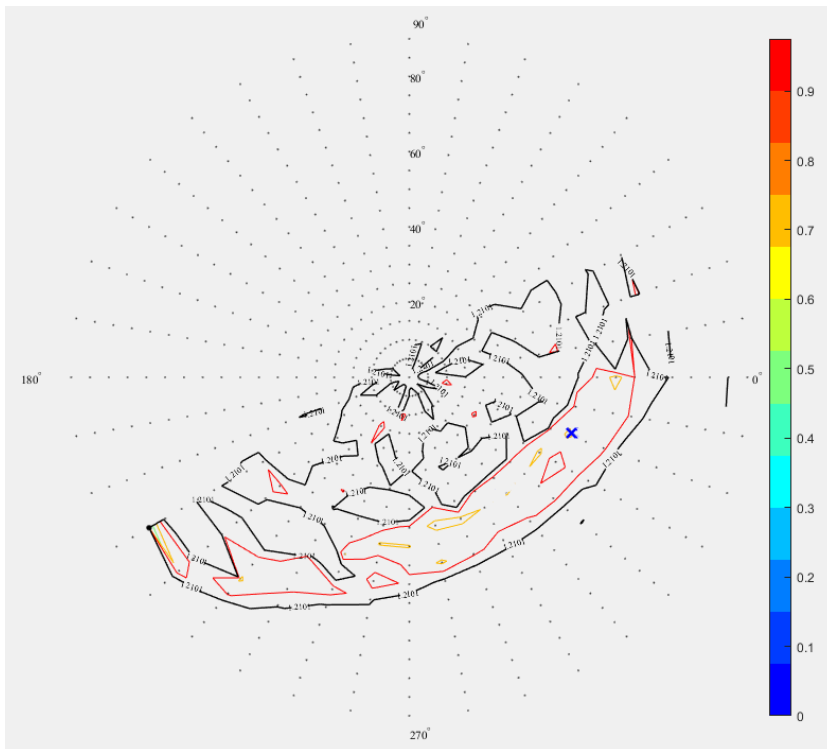
Fig. 3.7: Residue map of the magnetic cloud on 2004-11-09. The black contour lines display values equal to twice the minimum residue's value. The colored contours are additional contours of lower residues. The colors of the contours are accorded with the color bar. The blue cross points at Z-axis orientations taken for the reconstruction.
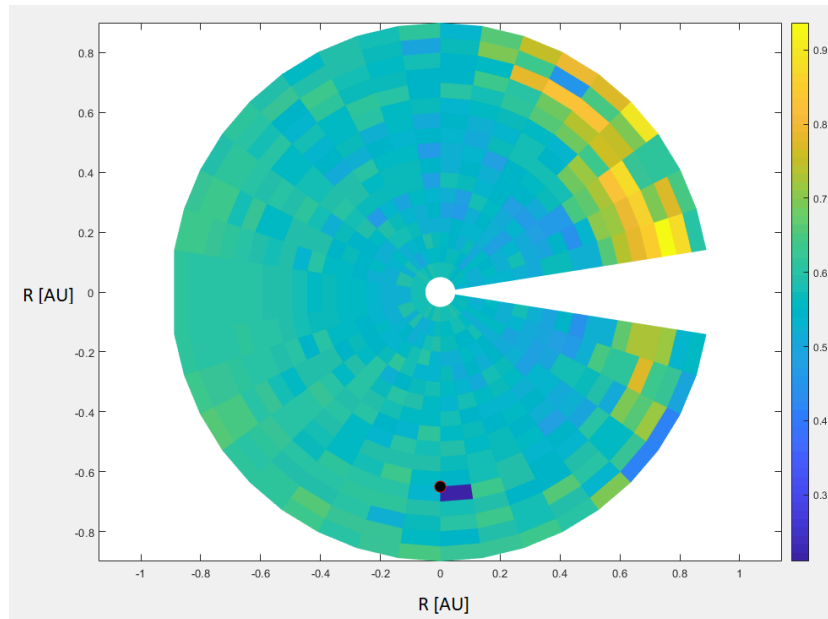
Fig. 3.8: This figure maps the ecliptic plane. The color map indicates the value of the residues considering the best Z-axis orientation at each point. The black dot points at the location where this residue reaches its minimum. The y and x-axis display lengths in AU. The values of the residues are detailed by the colorbar.

The first step indeed consists in trying every Z-axis orientation on every knot of the solar ecliptic grid. Figure 3.8 is showing this grid, on which the colors are a visualisation of the best residues found on each knot. The black dot is indicating the point where the best residue has been found. In fact, the figure 3.7 is a representation of the half-sphere over the point indicated by the black dot of the figure 3.8. In other words, the minimum residue is given by the Z-axis orientation of figure 3.7, and the Z-axis origin of figure 3.8.

It is for the moment not relevant to claim the Z-axis position, as it is still going to be calculated in the second step. However, this first step provides the Z-axis orientation. The results derived from that analysis are in very good agreement with those given in the paper by Isavnin et al. (2011) with $\theta = -29$ and $\phi = 45$, showing a difference of less than 7%.

3.2.3 Positioning the Z-axis

In this second step of the reconstruction, we find the Z-axis origin and derive the χ^2 and Q parameters describing the quality of the magnetic components's fit. The results give $\chi^2 = 0.441$ and $Q = 1$. Both of these parameters confirm the success of the reconstruction.
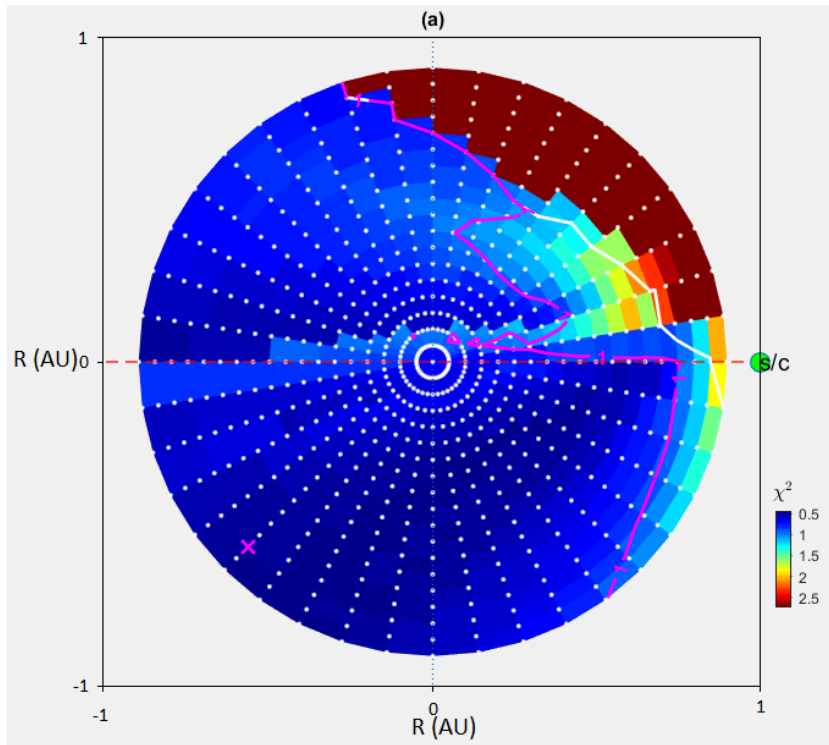
Fig. 3.9: Mapping of the solar ecliptic plane. The colormap shows the values of χ^2 at each points of the surface. The pink solid lines display the countour, where $\chi^2 = 1$. The pink cross is the best Z-axis origin found by the reconstruction.
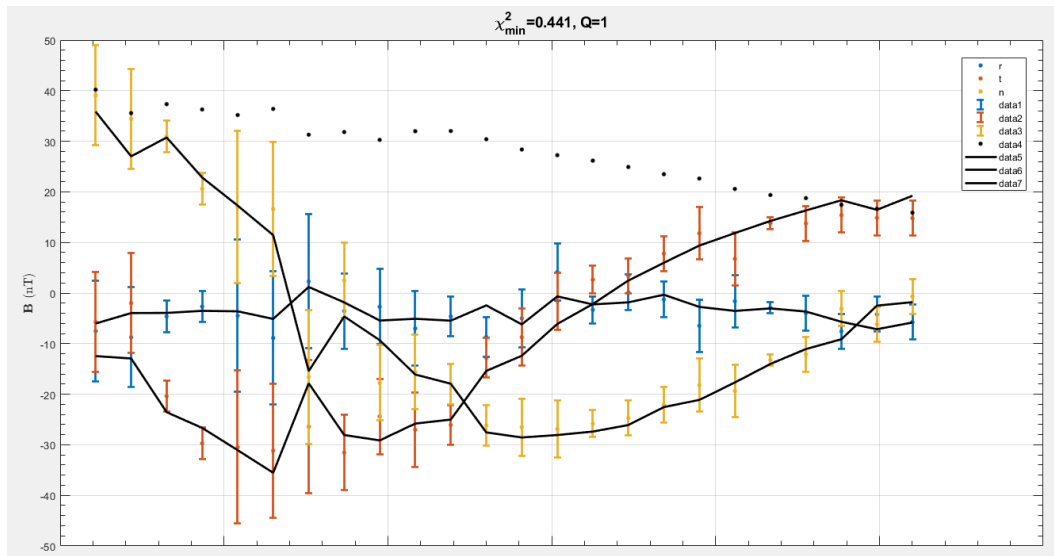
Fig. 3.10: The fit of the magnetic field components considering the Z-axis orientation and origin calculated previously. Each data point comes with its associated error-bar. The solid black line is the fitting line. The values of χ^2 and Q are revealed at the top of the plot.

In the figure 3.9, the pink cross indicates the position of the Z-axis origin according to the code's computations. This one is located at 1.41 AU of the spacecraft on the x-axis, and -1.37 AU of the spacecraft on the y-axis. Here, x and y are on the ecliptic plane. The major radius R_0 measures 1.38 AU. As for now, we have the best position of the Z-axis origin and the best Z-axis orientation. Nevertheless, we will verify the χ^2 and Q parameters.

Figure 3.10 shows the fit of the magnetic components. The data with the error-bars are interpolations of the real magnetic field, the errors being imported from CDAWeb and available in the data of the cloud. The solid black lines are showing the fits. The plot also indicates the two important parameters: $\chi^2 = 0.441$ and $Q = 1$. χ^2 is here relatively low, as a value of 2 is already considered to be a successful reconstruction (Hu, 2017). Moreover, the Q parameter tells us the probability of this χ^2 being the lowest possible. This probability, being one, means that our reconstruction is reliable.

3.2.4 Symmetry and reconstruction

This last part uses all the previous results to reconstruct the cross-section of the magnetic flux rope. After looking at the symmetry of the F function over the inward and outward branches, the GS-solver is used to obtain a contour plot of the isocontours of the F function in the flux rope cross-section.
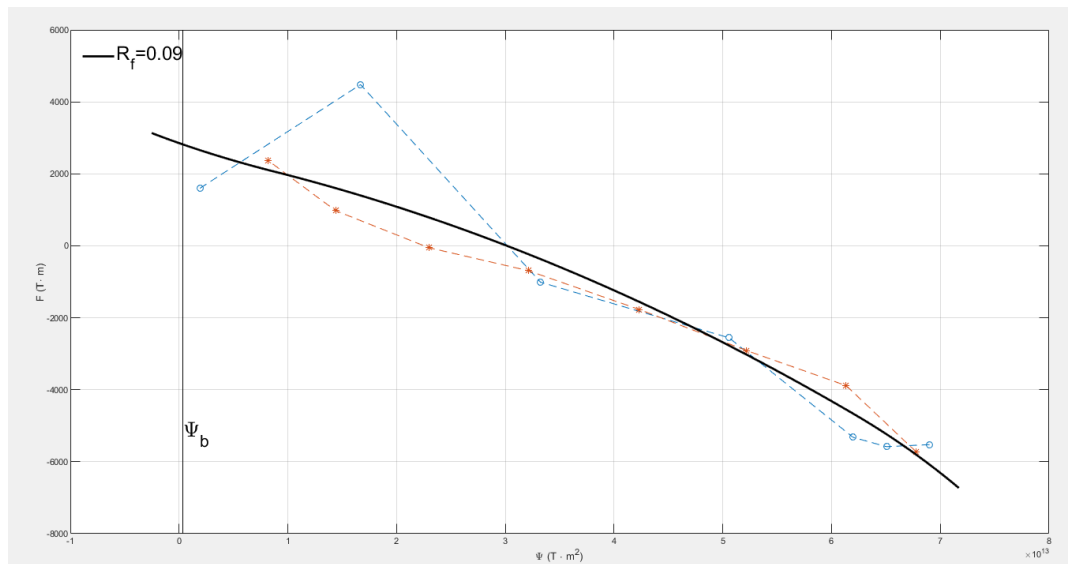
Fig. 3.11: This plot displays the values of $F(\Psi)$ measured during the inward (blue circles) and outward (red stars) motions of the spacecraft in the flux rope. The solid black line is the fit of these two lines and will be used for the reconstruction. The horizontal black line shows the selected single valued Ψ. The Ψ_b is the value of Ψ at the flux rope's boundary. R_f is the residue of the fit. The poloidal flux is equal to the width of the black fitting curve.

Figure 3.11 relates how symmetric the F function is. The circles are the inward values of F and the stars are the outward values of F. The black solid line is the fit of those two curves. The fit is made with a polynome of the third degree. $R_f = 0.09$ is the residue of this fitting. Residues under 0.2 are acceptable (Hu, 2017). In the article of Hu (2017), a noise level of 0.01 on a synthetic ideal magnetic flux rope yields a residue of $R_f = 0.1$. This noise level being small, we conclude that 0.1 is a low residue's value. Our reconstruction is, therefore, acceptable.

The parameters R_f, χ^2 and Q are valid. The calculated angles correspond to the results of Isavnin. The final step is to display the reconstruction of the flux rope's cross section. This reconstruction is shown in figure 3.12.
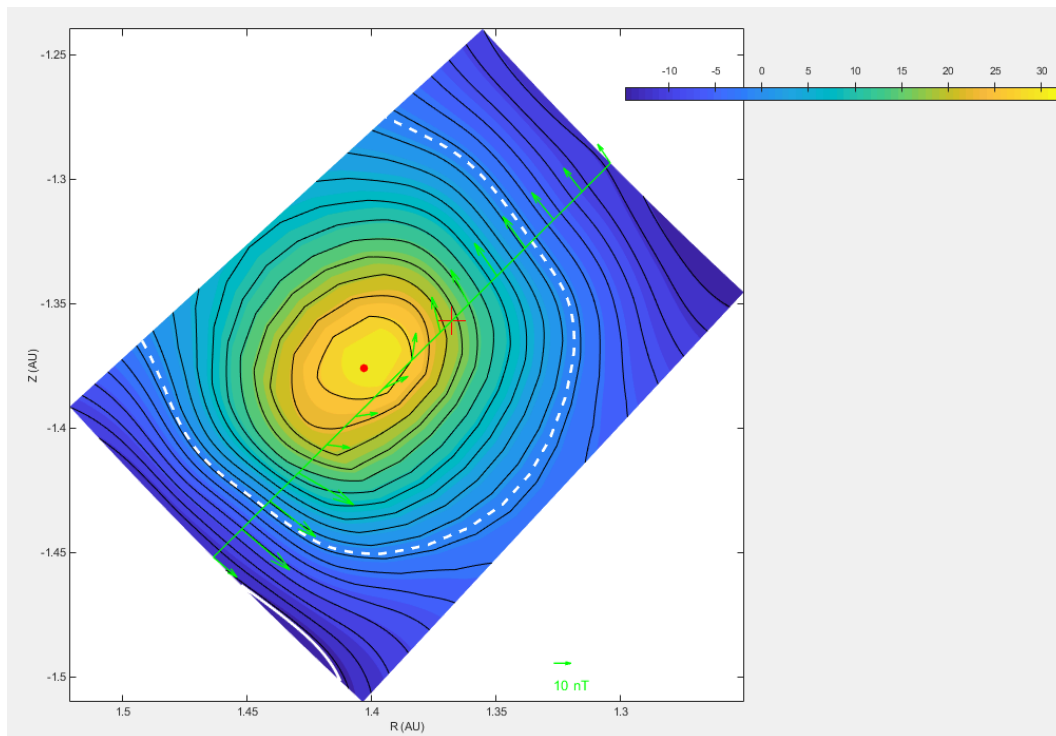
Fig. 3.12: Reconstruction of the cross section of the magnetic flux rope. The color map shows the magnetic field's strength in the z direction. The unit of the color bar is in nT. The solid green line is the path of the spacecraft. The green arrows are the magnetic field components in the (r,θ) plane. The red dot is the center of the flux rope. The white dotted line is the contour of Ψ_b.

With the solving of the Grad-Shafranov equation come several interesting parameter results.

The impact parameter is calculated to be 0.011 AU. In the article of Isavnin, the impact parameter has also been derived and equals 0.025 AU. It means, our impact parameter is more than two times smaller than the one derived in the paper, even though our angles are similar. Nevertheless, this does not mean that the results are false. Indeed, in the same article, two reconstructions are made. One with ACE data, and the other with WIND data. The difference in the impact parameter calculated is larger by 0.05 AU even after withdrawing

the distance between the two spacecrafts. This discrepancy can be explained by the fact that the method is based on ideal assumptions. These assumptions are not totally respected in reality. Moreover, the fluctuations of the data and the uncertainty of the selection of the flux rope boundaries may alter the results. Also, other methods as minimum variance analysis (MVA) give other Z-axis orientation. The difference reaches 40-50° for this event (Isavnin et al., 2011).

The toridal flux, the poloidal flux and B_{max} (the maximum of the magnetic field in the z direction) are additional outputs of the reconstruction. Here F_{tor} = 3.31 10^{12} T m^2, F_{pol} = 7.13 10^{13} T m^2 and B_{max} = −32 nT.

The reconstruction contains an additional function to reconstruct the appearance of the flux rope in three dimensions, as shown in figure 3.13. In this figure, the twist of the magnetic flux rope is visible. All the lines turn around the center of the flux rope. The twist increases with the distance to the center of the flux rope. Hence, the blue line is on the outside, the red line on the inside, and the pink one is located between the two previous lines. In fact, we could have understood this from figure 3.12. From the color map, we see that the strength of the magnetic field in the z direction increases near the center of the flux rope. On the other side, the green arrows represent the projection of the magnetic field on the cross section's plane. We notice that the arrows are larger (shorter) in the regions where the z-oriented magnetic field is weaker (stronger). That is, the magnetic field near the center is strong in the z direction and weak in the (r,θ) plane. These lines mainly contribute to the toroidal magnetic flux, as their twist is low. Whereas, further away from this center, the magnetic field is weak in the z direction and strong in the (r,θ) plane. In this region, the lines contribute to the poloidal magnetic field and their twist is high. We understand now why the figure 3.12 implies the figure 3.13.

The poloidal flux is over 10 times the toroidal flux. This can have several explanations. On the outer layers of the flux rope, the magnetic field lines have a higher twist and are mainly poloidal. We could imagine a new boundary on the flux rope cross section displaying where $\vec{B_l} \cdot \vec{e_z} = \sqrt{(\vec{B_l} \cdot \vec{e_r})^2 + (\vec{B_l} \cdot \vec{e_\theta})^2}$, i.e., where the toroidal magnetic field equals poloidal one. In reality, the $\vec{e_r}$ component of the field does not participate to the poloidal nor toroidal magnetic flux. Hence, the equation becomes: $\vec{B_l} \cdot \vec{e_z} = \vec{B_l} \cdot \vec{e_\theta}$ or $B_z = B_\theta$. Assuming that the flux rope has a symmetry under rotation in θ, we can locate this border with a parameter r_{eq}, distance from the center of the flux rope ($r = 0$). The surface that is going to dominate in the poloidal flux is then the surface within r_{eq}. Yet, the surface within r_{eq} decreases quadratically with this value. In turn, the rate at which the twist evolves inside the flux rope can largely influence the proportions of poloidal and toroidal fluxes. Moreover, the geometry of the flux rope can have an effect on the fluxes through flattening or pancaking effects (Riley and Crooker, 2004).

Additionally, the poloidal flux is integrated over the whole flux tube length. This length is one of the main uncertainties in deriving the poroidal flux. In short, the poloidal flux

depends on the total radius of the torus R, whereas the toroidal flux depends on the local radius of the flux rope r, itself dominated by the contribution within r_{eq}.
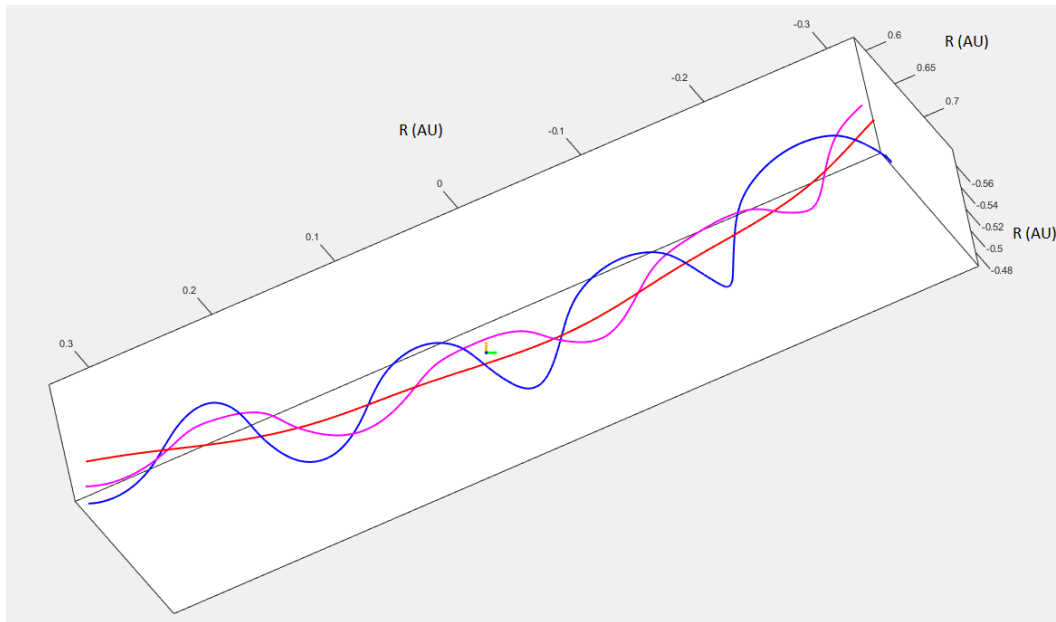
Fig. 3.13: 3D representation of the magnetic field lines. The lines turn around the center of the flux rope. We note that the twist increases when the magnetic field lines are further away from the center of the flux rope.

4

The influence of the boundary selection: the event on 2013-06-28

In this section, we are going to examine the consequences of the choice of the boundaries on the reconstruction. This choice has a large effect on the residue map of the Z-axis orientation, and on the position of this one on the ecliptic plane. Therefore, all the reconstruction parameters are influenced by such a modification.

To discuss the influence of the boundary selection, we will make several reconstructions of the same event with different boundary choices. We will compare the results with the values found by Al-Haddad et al. (2018). This article relates several reconstructions of the same event using several methods. Our reconstruction with the new code of Qiang Hu agrees with the results of Al-Haddad when the data are smoothed.

4.1 The data

A profound understanding of the data is crucial for choosing sensible boundaries. Previously, we discussed the characteristics of several parameters inside a flux rope. Those characteristics greatly restrict the choice of the boundaries. Nevertheless, a freedom remains in the choice of those boundaries. For example, in the previous CME event on 2004-11-09, whose duration extends up to 2173 minutes, the front boundary could be chosen within a time range of 165 minutes. Whereas, the time range in which we could have selected the rear boundary lasted 636 minutes. It seems that the inaccuracy of the selection of the rear boundaries is greater than the one of the front boundaries.
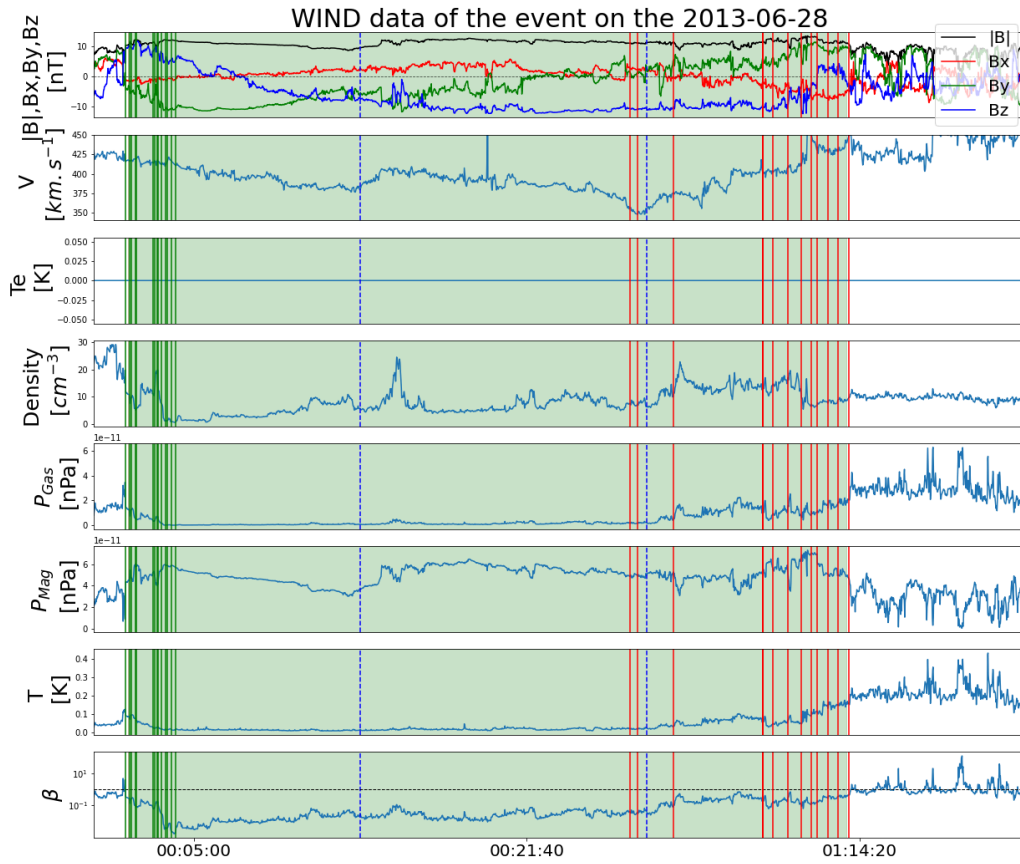
Fig. 4.1: The data of the cloud on 2013-06-28. From top to bottom: The magnetic field and its components, the cloud's velocity, the electron temperature, the proton density, the gas pressure, the magnetic pressure, the total temperature and the β parameter. The green area highlights the frozen-in region. The green and red vertical lines are every front and rear boundary used for the later reconstructions. The time on the x-axis is given with the format day:hour:minutes with 00:00:00 starting at the beginning of 2013-06-28.

At a first glance, we can immediately see that each magnetic field component is rotating. Indeed, the B_x component starts at 0 nT, rises up to 10 nT and then, falls back down to -10 nT. B_y, on its side, sweeps all values from -20 nT to 20 nT over the frozen-in region. Finally, B_z decreases strongly, and stabilises in a second time, when the two other components seem to accentuate their rotations.

Secondly, we see that the front boundary's range (green vertical lines on figure 4.1) is more restricted than the rear boundary's range (red vertical lines on figure 4.1). In fact, all the characteristics of a flux rope appear at the same time: While the magnetic field starts to be enhanced and smooth, the cloud velocity begins to decrease linearly. Simultaneously, the β parameter drops below one. All in all, the uncertainty of the front boundary of the flux rope is lower than the uncertainty of the rear one.

Indeed, one could take as rear boundary the point where the β parameter reaches one again. This would be the latest boundary possible. Another possibility is to follow the cloud

velocity, and to stop at the second blue dashed line. Notice that shortly after this blue dashed line, the β parameter gets closer to one. At the same point, the temperature, the magnetic pressure, the gas pressure and the density all show a spike. The gas pressure leaves its minimum at this exact point. This time is another possibility for the end of the flux rope.

In reality, we can almost distinguish two flux ropes from the magnetic field components. This claim is supported by the look of the cloud velocity curve. Precisely, the velocity V decreases two times linearly. One first time from the front boundary to the first blue dashed line, and a second time from the first to the second blue dashed line. Furthermore, at the start of the second linear decrease, we can see a spike in the density curve. This could be the remnant of a shock. Over those two regions, we could interpret the magnetic fields as rotating two times. In the first region, the components B_y and B_z rotate. Whereas, in the second region, the components B_x and B_y rotate.

In fact, we have tried to confirm this theory by reconstructing the two hypothetical flux ropes. At the end, the reconstruction proves that this event contains only one flux rope. Indeed, the function $F(\Psi)$ is not folded (does not present the two branches). This means that the code does not find a symmetry in the function $F(\Psi)$. In other words, no closed contours can be extrapolated from these boundaries. The event on the 2013-06-28 is a simple event with a single flux rope.

To summarize, the flux rope has a clear start, meaning that the range of the choice of the front boundary is short. The rear boundary can be assumed at different times depending on the parameters we are looking at. Also, the features of the magnetic field and the cloud velocity remind of two separate flux ropes. The Grad-Shafranov reconstruction tells us, however, that this event contains only one flux rope.

4.2 Comparing two different reconstructions

In order to understand how the differences manifest in the reconstructions, we are going to proceed to two reconstructions of the same cloud. Thereby, the boundaries are going to be different.

The first step is to take a successful reconstruction. To be sure, we will define as successful a reconstruction whose residues are low, χ^2 is under two, with a double folded $F(\Psi)$ function and with Z-axis angles near Al-Haddad's results: $\theta = -66$ and $\phi = 330$ (Al-Haddad et al., 2018).

The results of Al-Haddad are composed of three reconstruction methods. The circular-cylindrical fitting model (CCS), the Force free fitting model (FF) and the Grad-Shafranov model (GS). Here are their results for this cloud:

Model	θ (°)	ϕ (°)
CCS	283	-55
FF	240	-62
GS	330	-66

Table 4.1: Results of the reconstructions of the event on 2013-06-28 following three different reconstruction methods: Circular-cylindrical fitting model (CCS), Force free fitting model (FF) and Grad-Shafranov model (GS) (Al-Haddad et al., 2018).

Our reconstruction being a GS model, we should get close to the GS reconstruction's results of Al-Haddad.

The green boundaries in figure 4.2 are those of our successful reconstructions. These boundaries are chosen as they give the closest results to the article's ones. The red boundaries of figure 4.2 represent the boundaries chosen for the second (or test) reconstruction. The differences in the results of those two boundary choices are studied.
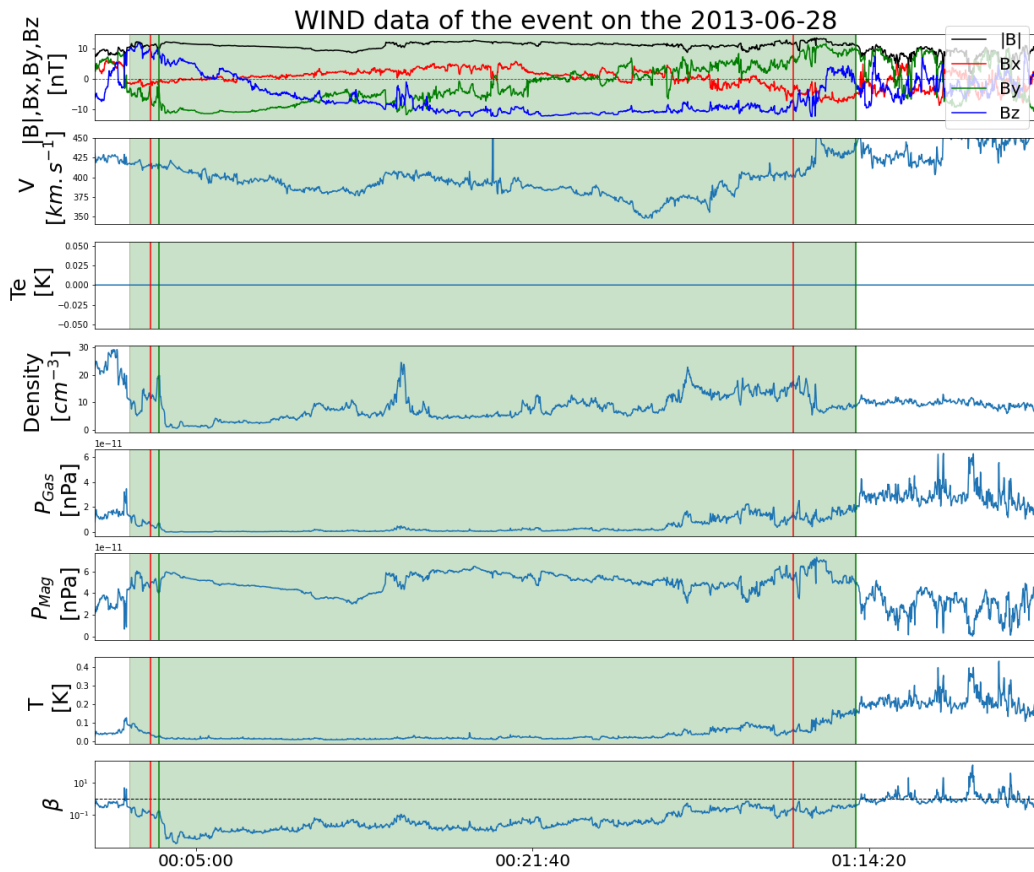
Fig. 4.2: Data of the cloud on 2013-06-28. The green highlighted area is the region where the β parameter is below one. The two colored vertical lines stand for the boundaries of the two test reconstructions. The green boundaries limit the successful reconstruction, whereas the red boundaries refer to the test reconstruction.

The figure 4.3 shows how we have selected the Z-axis orientation. Indeed, in the purpose to get as close as possible to the results of Al-Haddad, we have marginally manipulated the procedure. Here, the Z-axis orientation has been slightly shifted compared to the ideal choice of the Z-axis orientation in the residue map. By doing so, the Z-axis orientation agrees with the Grad-Shafranov results of Al-Haddad (see table 4.1). With this Z-axis orientation, we verify that the other reconstruction parameters χ^2 and Q are acceptable.
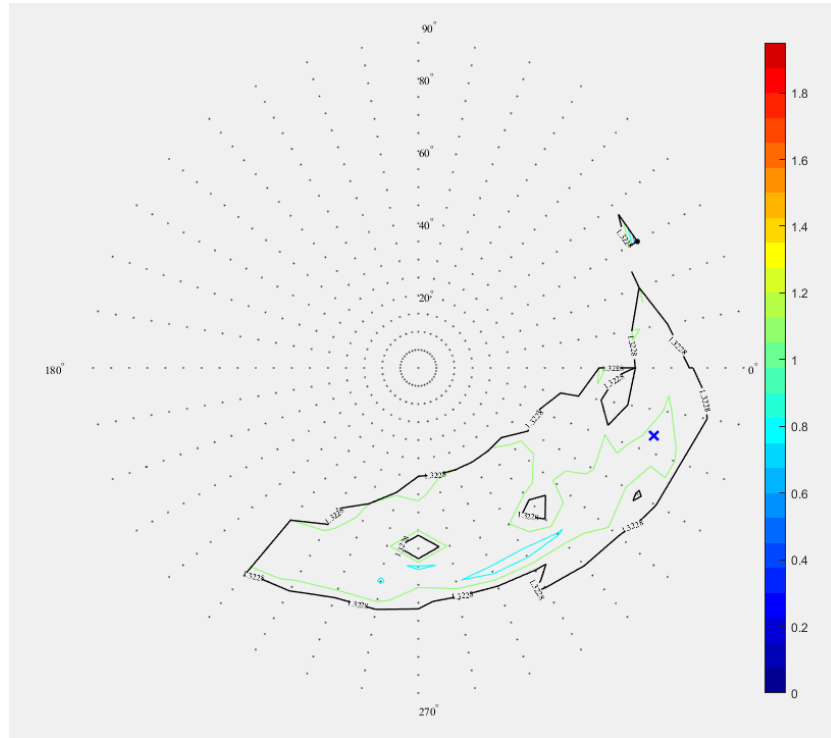
Fig. 4.3: Residue map of the successful reconstruction. The black solid line is the contour of twice the minimum residue. The colored contours have levels associated with the color bar. The blue cross represents the selected Z-axis orientation.

As a matter of fact, the results are highly satisfying. This reconstruction yields a χ^2 of 0.885 and a Q of 0.724. Recalling that a χ^2 under two was considered a successful reconstruction. The inward and outward branches of the F function are folded, and the residue of the fit is 0.09, which is below 0.2, and therefore, accepted. Last but not least, the reconstruction map contains all the expected characteristics, i.e. the isolines of $F(\Psi)$ are closed inside the flux rope's boundary, it contains a point of maximal toroidal magnetic field at the center of the closed contour lines. Note that, in the article of Al-Haddad, the aspect ratio was also given as output. The aspect ratio is the ratio of the flux rope's radius over the major radius ($\frac{r_0}{R_0}$). Our reconstruction does not give the aspect ratio explicitly. However, we can approximate it with the reconstruction map and the calculated major radius. Our major radius in this reconstruction is 0.8847 AU. Here, in the reconstruction map of figure 4.5, we can guess the radius of the flux rope, being the radius of the white line circle. The size of the axes are approximately 0.4 AU and, to be sure, we can limit the size of the flux rope by

0.25 AU from beneath. Therefore, we can say, without much risk, that the size of the flux rope is 0.325 ± 0.075 AU. The aspect ratio is then 0.37 ± 0.09 AU. This is the half of 0.8 AU, which is the result of Al-Haddad.
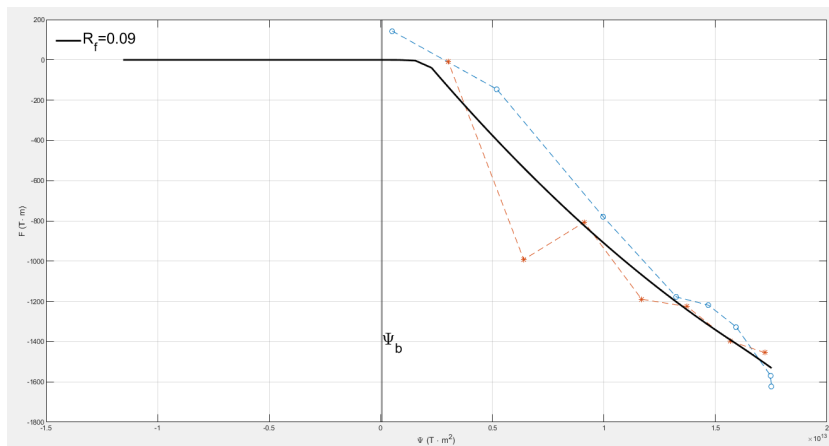
Fig. 4.4: Fit of the inward and outward measurements of $F(\Psi)$ of the successful reconstruction. The black solid line represents the fit of the two colored branches. R_f is the residue of the fitting cruve. The black vertical line is the value of Ψ at the boundary of the flux rope.
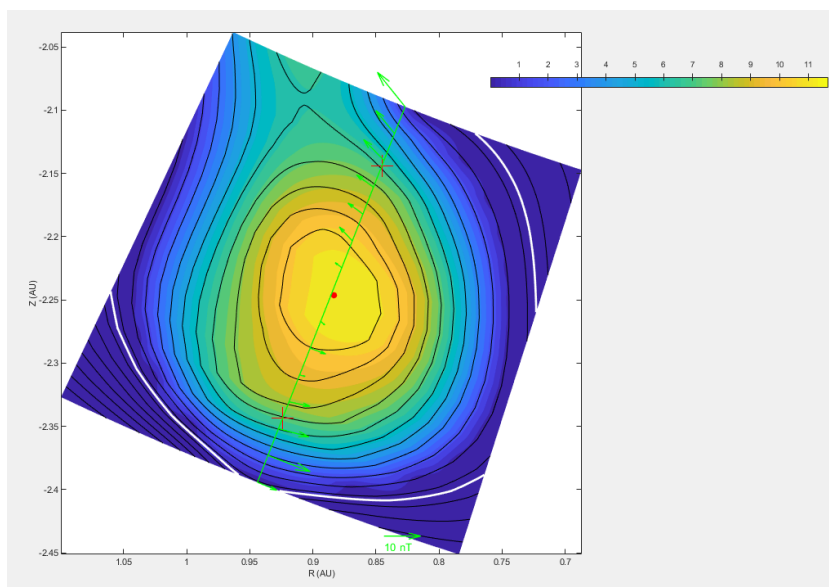
Fig. 4.5: Flux rope cross section of the successful reconstruction. The two red crosses point at the locations where $B_z = \sqrt{B_r^2 + B_\theta^2}$. The color map, associated with the color bar, displays the z component of the magnetic field. The black contours are the contours of $F(\Psi)$. The red dot is the center of the flux rope. The green solid line is the path of the spacecraft. The green arrows are the magnetic field components in the plane of the cross section.

Figures 4.6, 4.7 and 4.8 are the principal results of the second reconstruction. The main differences between the test reconstruction and the second one is the apparent global rotation

of the residue islands in figure 4.6. As for the previous reconstruction, the axis orientation has been shifted, in order to make a compromise between the residue map results and the results that we are supposed to obtain from a GS reconstruction. This procedure is not outrageous as the Z-axis orientation has been selected among the minimal residue island present on this map in green (see figure 4.6). Nonetheless, the outcoming Z-axis orientation present a 27% difference with the results of the Al-Haddad, and up to 28% with our previous results.
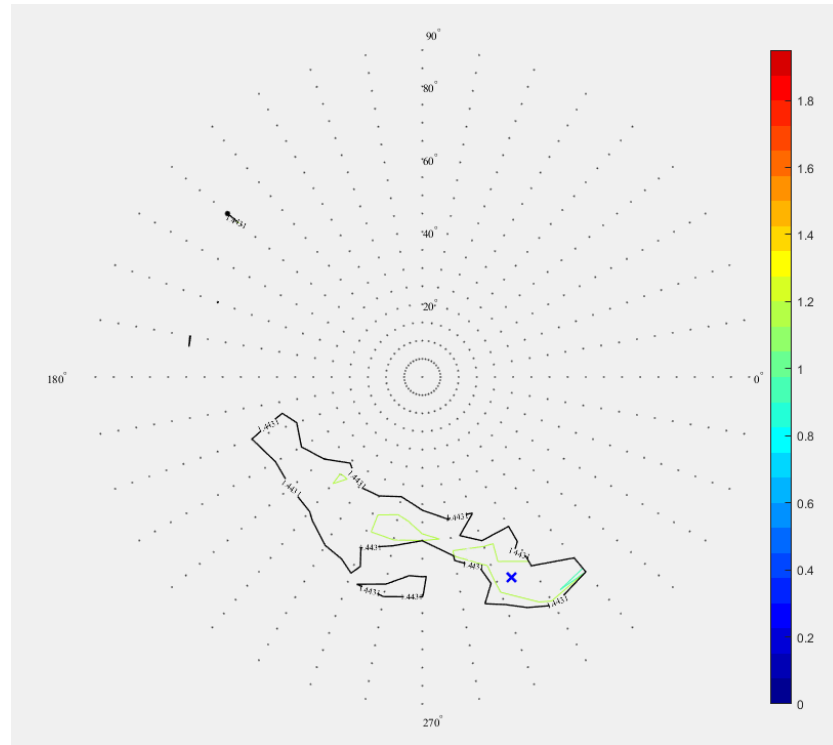
Fig. 4.6: Residue map of the test reconstruction.

The figures 4.4 and 4.7 look quite similar. The single valued Ψ_b is, in both cases barely over 0, and the fitting curves have a similar appearance. Yet, these curves span over different ranges. The range of the curve on the x-axis equals the poloidal flux. Our original test has $F_{pol} = 1.75\ 10^{13}$ T m^2, whereas the second reconstruction yields a poloidal flux of $F_{pol} = 1.15\ 10^{13}$ T m^2. This is a consequence of the difference of tilt of the curves. The direct effect that this flatter curve has on the reconstruction map is the elongation of the flux rope. On the reconstruction map of figure 4.8, we have to be careful with the x and y axes's scales. The y-axis covers a distance of 0.15 AU while the x-axis covers a range of 0.25 AU. The figure is not on scale and we have to imagine the structure almost two times brighter in the x-direction. This elongation is not unknown from the scientists. Magnetic flux ropes often elongates in the direction of motion of the cloud (Möstl et al., 2009). A curious output of this reconstruction is that the final residues are lower than our success-

ful reconstruction, as it equals 0.06 for these boundaries instead of 0.09 for the previous ones.
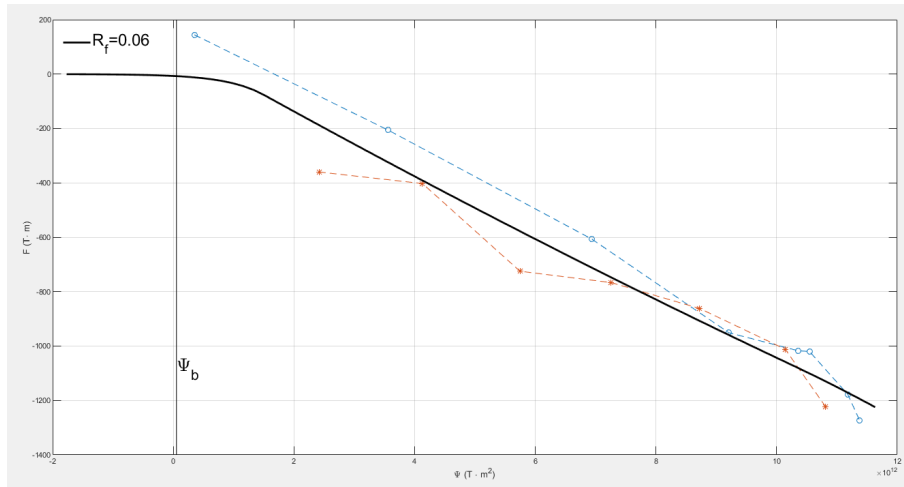
Fig. 4.7: Fit of the inward and outward measurement of $F(\Psi)$ for the test reconstruction.
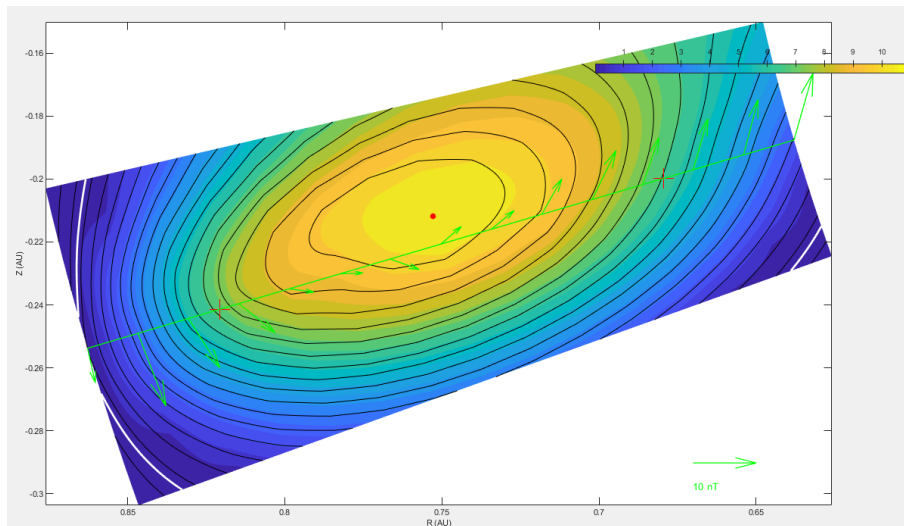
Fig. 4.8: Cross section of the flux rope for the test reconstruction.

Table 4.2 shows the accuracy of the reconstructions. Even though the change on the boundaries makes sense, the results of this second reconstruction show large uncertainties. Indeed, the χ^2 equals two. Which is, as we already discussed, the upper acceptable value for this parameter. Q is really low here, even if we do not have any references on what should be a valid Q. Moreover, it turns out that, in some reconstructions, the Q is under $\frac{1}{2}$ when the χ^2 is below 1.

For such a boundary shift, the discrepancies in the angles are enormous. The θ angle changes by 17 degrees, or 25%. The ϕ angle changes by 91 degrees, or 27% (see table 4.3).

$N°$	Start (DOY:H:Min)	Duration (D:H:Min)	χ^2	Q	R_f
a	179:02:45	1:07:50	2	0.1	0.06
b	179:03:10	1:10:39	0.885	0.724	0.09

Table 4.2: Reconstruction quality parameters of the test (a) and the successful (b) reconstructions.

$N°$	θ	ϕ	R_0	b	B_{max}	F_{pol}	F_{tor}
Unit	°	°	AU	AU	nT	10^{13}T m^2	10^{13}T m^2
a	-50	243	0.75	0.01	-10.9	0.276	1.16
b	-67	334	0.88	0.002	-11.6	0.108	1.75

Table 4.3: Output parameters of reconstruction giving information on the cloud for the test boundaries (a) and the successful one (b).

4.3 Study on 17 reconstructions

From 17 different reconstructions having 17 different boundaries, we calculated a weighted average of the output and quality parameters. The two resulting Z-axis angles are $\phi = -64°$ and $\theta = 247°$. These results disagree with the results of Al-Haddad. In fact, this would mean that our results are closer to the FF model than to the GS one.

The 17 reconstructions have been selected for having a χ^2 under two. All reconstructions have final residues inferior to 0.12, and in all cases, the $F(\Psi)$ function was double folded and symmetrical. The results of these reconstructions can be found in tables 4.4 and 4.5.

4.3.1 Comparison to the results of Al-Haddad et al. (2018)

The reconstruction is based on the symmetry that exists within the composed $F(\Psi)$ function. This function folds on itself. One branch represents the inward movement of the spacecraft, the other its outward movement. As the contours of F are circling around the center of the flux rope, each value of F that the spacecraft is crossing during its inward path should also be crossed during its outward path.

Guided by this idea, we will consider the final residue as the best indicator of a successful reconstruction. A χ^2 under two is also going to be important for the validity of the reconstruction. Q does, however, not tell us that the reconstruction is false. It is merely a probability of having the best reconstruction possible.

To derive more objective results we introduce a weighted average for the goodness of the reconstruction. Indeed, we want the final residue R_f to define the strength of the weight.

N°	Start (DOY:H:Min)	Duration (D:H:Min)	χ^2	Q	R_f
1	179:01:36	01:09:49	1.44	0.01	0.07
2	179:01:43	01:10:22	0.506	0.996	0.07
3	179:01:47	01:01:26	0.847	0.089	0.06
4	179:01:54	01:02:38	1.28	0.03	0.06
5	179:02:05	01:02:56	0.702	0.999	0.04
6	179:02:08	1:07:51	0.916	0.729	0.03
7	179:02:45	1:07:50	2	0.1	0.06
8	179:02:59	1:09:13	0.692	0.835	0.07
9	179:02:55	1:08:55	1.25	0.118	0.12
10	179:03:10	1:10:39	1.64	0.01	0.11
11	179:03:13	1:06:17	0.929	0.877	0.12
12	179:03:24	1:06:06	1.12	0.618	0.05
13	179:03:35	1:07:10	0.546	0.278	0.13
14	179:03:40	1:09:35	0.527	1	0.07
15	179:03:53	1:05:37	0.403	1	0.12
16	179:04:05	1:08:41	0.885	1	0.05
17	179:04:25	1:07:25	0.731	0.841	0.11
$\bar{w}$	179:02:40	1:07:03	0.930	0.610	x

Table 4.4: Results of the quality of the 17 reconstructions of the event on 2013-06-28. DOY means Day of Year, H, hour and Min, minutes. The duration has the same format. The line following $\bar{w}$ is a simple average of the data of the 17 reconstructions.

Therefore, we can write:

$$\bar{w} = \bar{\delta} + \bar{v} \tag{4.1}$$

In equation 4.1, $\bar{w}$ is our weighted average, $\bar{\delta}$ is the difference to the average and $\bar{v}$ is the average of the value we are studying.

$$\bar{\delta} = \frac{\sum_{j=1}^{N}(v_j - \bar{v})(\frac{1}{R_j} - 5)}{\sum_{i=1}^{N}(\frac{1}{R_i} - 5)} \tag{4.2}$$

In equation 4.2, v_j are the values for each reconstructions, R_j are the residues associated with the values v_j. Our weight is $\frac{1}{R_i} - 5$.

We want that the weight vanishes if the residue of a reconstruction equals 0.2, as it is the limit of an acceptable reconstruction. $\frac{1}{R_j} - 5 = 0$ for $R_j = 0.2$. Note that $\bar{\delta}$ is never infinite as the denominator is the sum of all weights, and does not vanish if at least one weight is different from 0.2. Naturally, as 0.2 being the worst acceptable solution, we expect to

$N°$	ϕ	θ	R_0	b	B_{max}	F_{tor}	F_{pol}
Unit	°	°	(AU)	(AU)	(nT)	(10^{13}T m^2)	(10^{13}T m^2)
1	−55	282	1.11	0.005	−11.43	0.523	2.29
2	−67	303	0.60	0.006	−11.65	0.661	1.33
3	−53	221	0.67	0.004	−11.42	0.276	1.23
4	−58	259	0.73	0.01	−10.83	0.349	1.36
5	−66	87	0.81	0.011	−11.27	0.334	1.73
6	−70	283	1.12	0.002	−12.02	0.501	2.69
7	−50	243	0.75	0.010	−10.90	0.276	1.16
8	−70	304	0.66	0.010	−11.76	0.682	1.39
9	−50	253	0.59	0.003	−10.54	0.443	0.903
10	−67	334	0.88	0.002	−11.60	0.108	7.75
11	−48	237	0.64	0.015	−10.31	0.409	0.879
12	−55	248	0.37	0.001	−11.80	0.316	0.646
13	−49	225	0.70	0.006	−11.13	0.455	0.925
14	−75	280	0.76	0.012	−11.64	0.627	1.63
15	−63	290	0.63	0.018	−11.02	0.548	0.855
16	−69	279	1.23	0.000	−11.99	0.673	2.48
17	−65	417	0.307	0.001	−10.19	0.363	3.31
$\bar{w}(m = 2.04)$	−64	247	0.86	0.005	−11.57	0.446	1.94
$\bar{w}(m = 29.6)$	−70	283	1.13	0.002	−12.02	0.501	2.69

Table 4.5: Output parameters of the 17 reconstructions of the event on 2013-06-28. The lines called $\bar{w}$ represent the weighted averages for different values of m.

have several residues below this value. If one R_j equals 0.2, $\delta_j = \frac{(v_j - \bar{v})(\frac{1}{R_j} - 5)}{\sum_{i=1}^{N}(\frac{1}{R_i} - 5)} N = 0$, and the associated reconstruction does not influence the average.

On the other side, we are going to derive what happens if one residue tends towards 0. Obviously, $\frac{1}{R_l}$ tends to infinity when R_l vanishes. But more importantly, if one of the residue vanishes, the associated weight will take over the others. Mathematically:

$$lim_{R_l \to 0} \sum_{j=1}^{N}(v_j - \bar{v})(\frac{1}{R_j} - 5) \to (v_l - \bar{v})(\frac{1}{R_l} - 5) \tag{4.3}$$

Here R_l is the residue that vanishes and is included into the R_js. Symmetrically:

$$lim_{R_l \to 0} \sum_{j=1}^{N}(\frac{1}{R_j} - 5) \to (\frac{1}{R_l} - 5) \tag{4.4}$$

Using equations 4.3 and 4.4 in equation 4.2, we find $\bar{\delta} = (v_l - \bar{v})$ and therefore, $\bar{w} = (v_l - \bar{v}) - \bar{v} = v_l$. This result is satisfying for two reasons. The first is that if one of the residue is null, the weighted average will not exceed the value associated with the vanishing

residue. The other reason is that this average will simply become the value associated with the vanishing residue. In other words, $\bar{w}$ is not ill-behaved and always tends to the best value.

Of course, there is an infinity of possible weights to take. For example, the weights $(\frac{1}{R_j^m} - 5^m)$, for any positive m, would have the same properties as the original weight. In fact, a higher m will give more influence to low residues. The weighted average tends faster towards the values associated with the lowest residues. We could have also not used weights at all, and compute a simple average of each output parameter. In this case, the quality of the reconstruction would not have been taken into account at all.
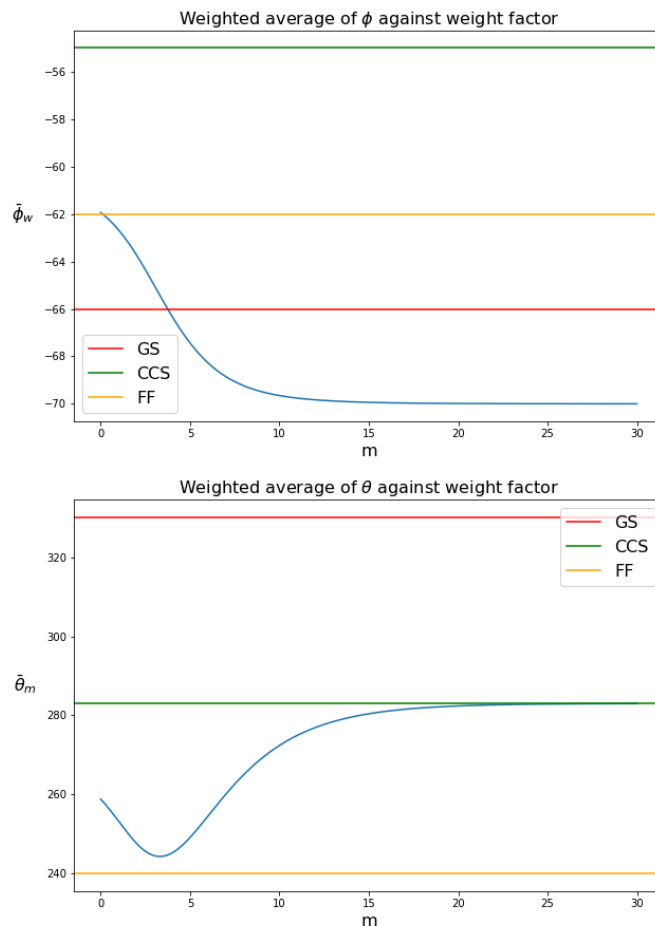
Fig. 4.9: Top panel: The blue line profiles the weighted averages of ϕ with respect to the degrees of m. Bottom panel: The blue line profiles the weighted averages of θ with respect to the degrees of m. In both plots, the red, yellow and green lines are the values of ϕ or θ in the GS, FF and CCS models, respectively.
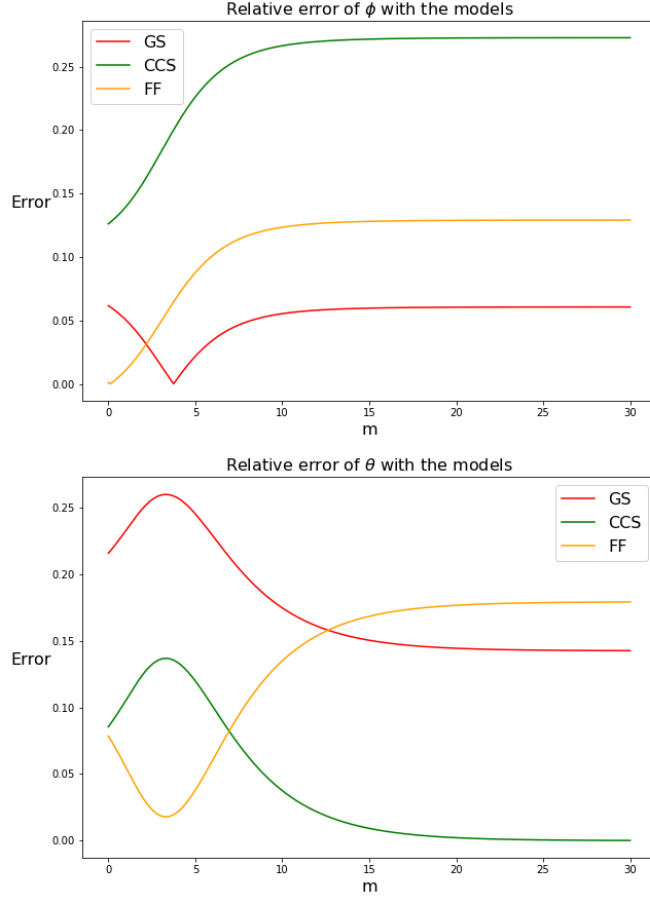
Fig. 4.10: In both panels, the red, yellow and green lines are the error profiles (ratio of the difference over the results of Al-Haddad) of the weighted averaged angles (for each degree of *m*) with respect to the GS, FF and CCS results of Al-Haddad, respectively.

In reality, we can compute the weighted averages of the values with respect to different weights. Figure 4.9 shows the weighted averages of ϕ ($\bar{\phi}_w$) and θ ($\bar{\theta}_w$) for different degrees *m* of the weight mentioned previously. The three horizontal lines are the values of ϕ and θ that Al-Haddad found in each model (GS, CCS, FF). Then, the figure 4.10 shows the relative error between our results and each of the model's angles. We define the total relative error as the average of the errors on both angles: $Err_{tot}^{model} = \frac{1}{2}(Err_\phi^{model} + Err_\theta^{model})$. With this, the minimum error for each model is:

$Err_{tot}^{GS} = 10.2\%$ for $m = 29.6$
$Err_{tot}^{CCS} = 10.6\%$ for $m = 0$
$Err_{tot}^{FF} = 3\%$ for $m = 2.04$

The minimum error (3%) is found in the FF model for $m = 2.04$. Our angles with a $m = 2.04$ are $\phi = -64°$ and $\theta = 247°$.

Hence, without any assemption on the strength of the weight, our results seem to confirm the FF model, and not the GS one.

4.3.2 The influence of the boundary selection

One of the goals of these 17 reconstructions was to find the influence of the choice of the boundaries on the ϕ and θ angles. Figure 4.11 contains the information regarding this influence.
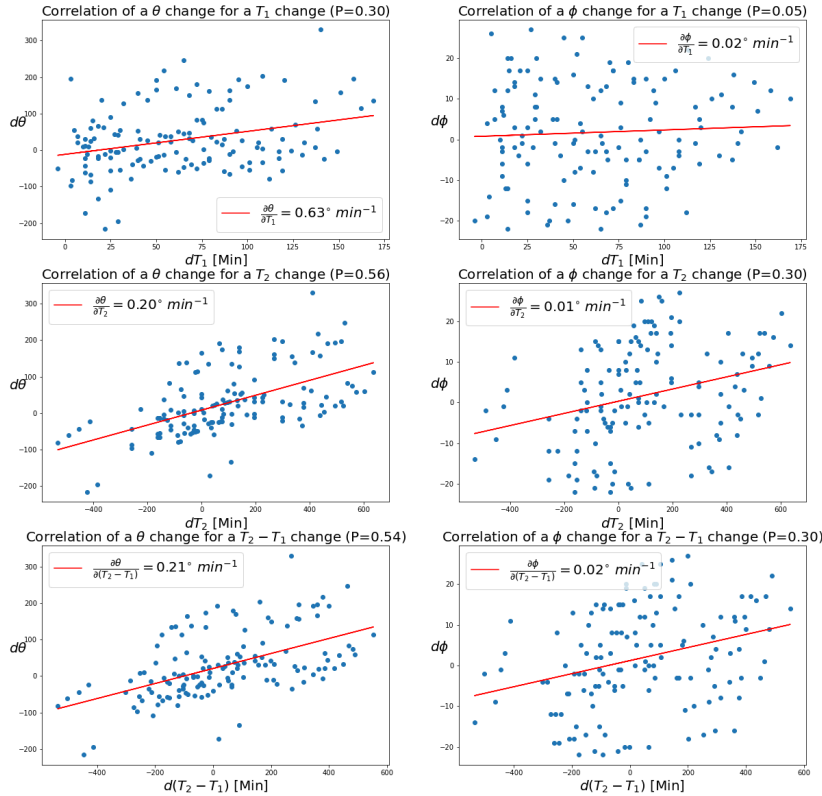
Fig. 4.11: The first column of plots concerns the variable θ. The second column concerns ϕ. The first, the second and the third lines plot the differences in the angles with respect to the differences on the front boundary, rear boundary and cloud duration, respectively. The red curves are the fitting curves of the data points. The legends display the tilt of the curve in the unit degrees per minute. P is the Pearson correlation coefficient.

The data points have been created from every possible combination of differences that one can obtain from the 17 reconstructions. P is the Pearson correlation coefficient. A low correlation coefficient means that a possible linear relation between the parameters (red in figure 4.11) is not very strong. We can deduce with relatively high reliability that the boundary choice has a greater influence on θ than it has on ϕ. However, the time range of choice for the front boundary is shorter than the one for the rear boundary. This means that the value of $\frac{\partial\theta}{\partial T_1} = 0.63°$ min^{-1} will be integrated over a shorter time as the value of $\frac{\partial\theta}{\partial T_2} = 0.20°$ min^{-1}. Overall, we can say that the choice on the rear boundary will have a great influence on the θ angle.

On the other side, for this cloud, the influence of the duration is equal to the influence of the

second boundary. We could expect this result, regarding the fact that the range of the rear boundary is much greater than the front one. The differences on the rear boundary selection will almost entirely define the differences in duration of the cloud.

4.4 Reconstruction from smoothed data

We now show how data smoothing affects the results. For that, we used a smoothing over two hours. The results of the reconstructions for the smoothed data confirm the results of the Al-Haddad study. Indeed, with the best degree of m being 0, the angles of the Z-axis are $\phi = -65°$ and $\theta = 330°$. These results have an average error of 0.7% with the results of Al-Haddad.

Smoothing the data has an impact on the statistics of the reconstructions. The goodness of fit decreases slightly from 0.930 without to 0.916 with the smoothing. However, the Q parameter increases significantly from 0.610 without to 0.916 with the smoothing. Additionally, the residues are overall lower with the smoothing. The results of these reconstructions are shown in tables 4.6 and 4.7.

$N°$	Start (DOY:H:Min)	Duration (D:H:Min)	χ^2	Q	residue
1	179:01:36	01:09:49	0.31	1	0.08
2	179:01:43	01:10:22	0.459	0.997	0.07
3	179:01:47	01:01:26	0.497	0.996	0.05
4	179:01:54	01:02:38	0.263	1	0.05
5	179:02:05	01:02:56	0.322	1	0.05
6	179:02:08	1:07:51	0.859	0.698	0.04
7	179:02:45	1:07:50	0.44	1	0.04
8	179:02:59	1:09:13	0.264	1	0.04
9	179:03:00	1:07:15	0.616	0.988	0.06
10	179:03:10	1:10:39	1.14	0.258	0.06
11	179:03:13	1:06:17	0.083	1	0.06
12	179:03:24	1:06:06	0.366	1	0.04
13	179:03:35	1:07:10	0.815	0.764	0.14
14	179:03:40	1:09:35	0.442	0.998	0.10
15	179:03:53	1:05:37	0.732	0.891	0.05
16	179:04:05	1:08:41	0.469	0.998	0.09
17	179:04:25	1:07:25	0.435	0.999	0.07
$\bar{w} = 1$	179:02:40	1:07:03	0.490	0.916	x

Table 4.6: Results of the quality of the 17 smoothed reconstructions of the event on 2013-06-28. DOY means Day of Year, H hour and Min minutes. The duration has the same format, except that DOY becomes D for Days, and the overall measure is a duration, not a date.

N°	ϕ	θ	R_0	b	B_{max}	F_{tor}	F_{pol}
Unit	°	°	(AU)	(AU)	(nT)	(10^{13}T m^2)	(10^{13}T m^2)
1	−73	397	0.30	0.014	−10.61	0.607	0.672
2	−66	298	0.76	0.005	−11.62	0.637	1.66
3	−66	242	1.43	0.012	−11.83	0.317	3.01
4	−62	282	0.94	0.003	−12.02	0.348	1.86
5	−64	278	1.29	0.006	−12.04	0.396	2.59
6	−76	376	0.17	0.029	−10.03	0.819	0.457
7	−58	304	1.00	0.008	−11.75	0.571	1.98
8	−69	313	1.20	0.0	−11.97	0.820	2.64
9	−66	266	0.71	0.006	−11.46	0.460	1.41
10	−73	313	0.62	0.096	−11.58	1.01	1.62
11	−79	405	0.46	0.017	−10.69	0.459	1.49
12	−51	321	0.86	0.018	−11.49	0.537	1.99
13	−45	470	1.41	0.037	−10.51	0.432	0.643
14	−64	418	0.40	0.01	−11.18	0.503	1.13
15	−44	366	0.73	0.027	−11.15	0.541	1.26
16	−70	447	0.74	0.007	−11.50	0.581	0.855
17	−80	424	0.122	0.02	−11.38	0.785	2.21
$\bar{w}(m=1)$	−65	328	0.842	0.017	−11.41	0.589	1.71
$\bar{w}(m=0.63)$	−65	330	0.838	0.017	−11.40	0.487	1.70

Table 4.7: Output parameters of the 17 smoothed reconstructions of the event on the 2013-06-28. The lines with $\bar{w}$ represent the weighted averages.

4.4.1 Comparison to the results of Al-Haddad et al. (2018)

The same analysis has been made as with the original data. From this study, we can plot ϕ and θ with respect to the orders of m of the weight (see figures 4.12 and 4.13). The best relative errors with respect to the models are:

$Err_{tot}^{GS} = 0.7\%$ for $m = 0.63$

$Err_{tot}^{CCS} = 14.2\%$ for $m = 5.65$

$Err_{tot}^{FF} = 17.8\%$ for $m = 5.44$

Once again, these results do not depend on the strength of the weight. We let the weight vary to obtain the best results. It turns out that this coefficient gives us information on the meaning of R_f. Indeed, our weight depends on R_f. A higher degree of m empowers the lower residues. Hence, the fact that we found the best error (0.7%) with a m that equals 0.63 tells us that, in this case, the parameter R_f does not summarize efficiently the quality of the reconstruction.

This time, The GS reconstruction seems to be the most accurate and agrees with the results of Al-Haddad. We have used the same boundaries as in the study of the original data.

Therefore, the increase in the quality of the results comes from the smoothing process.
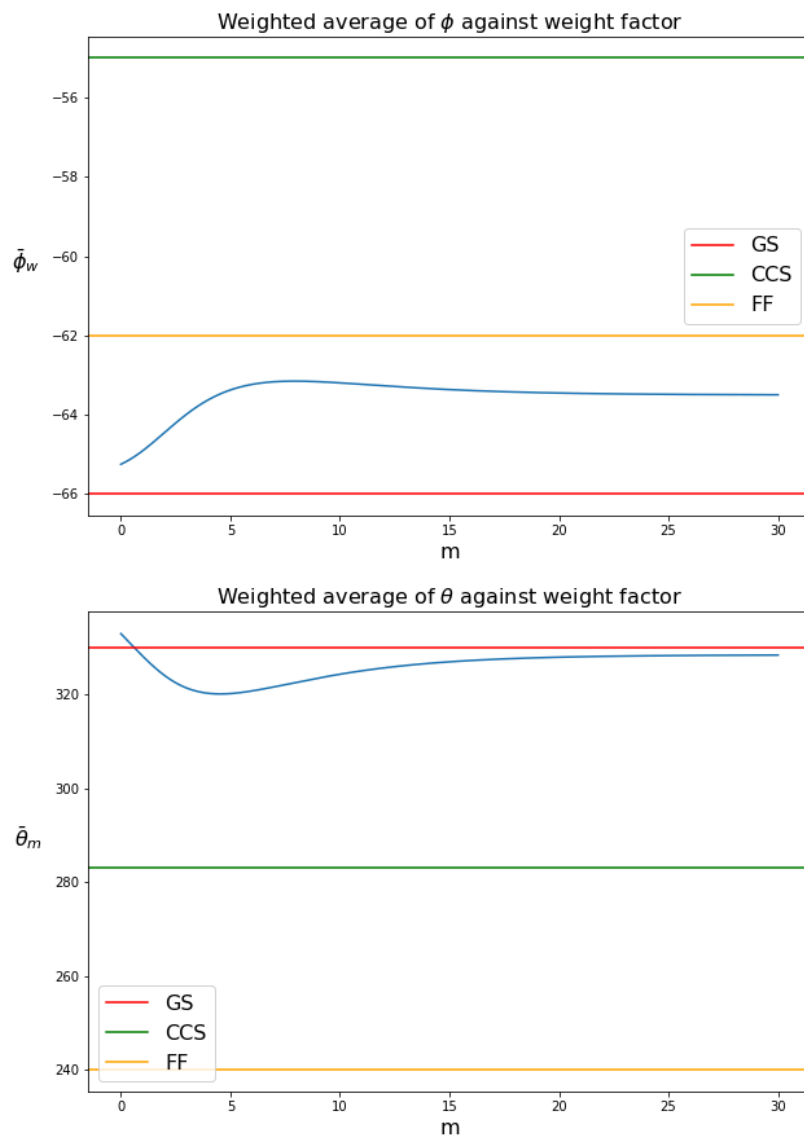
Fig. 4.12: Top panel: The blue line profiles the weighted averages of ϕ with respect to the degrees of m. Bottom panel: The blue line profiles the weighted averages of θ with respect to the degrees of m. In both plots, the red, yellow and green lines are the values of ϕ or θ in the GS, FF and CCS models, respectively.
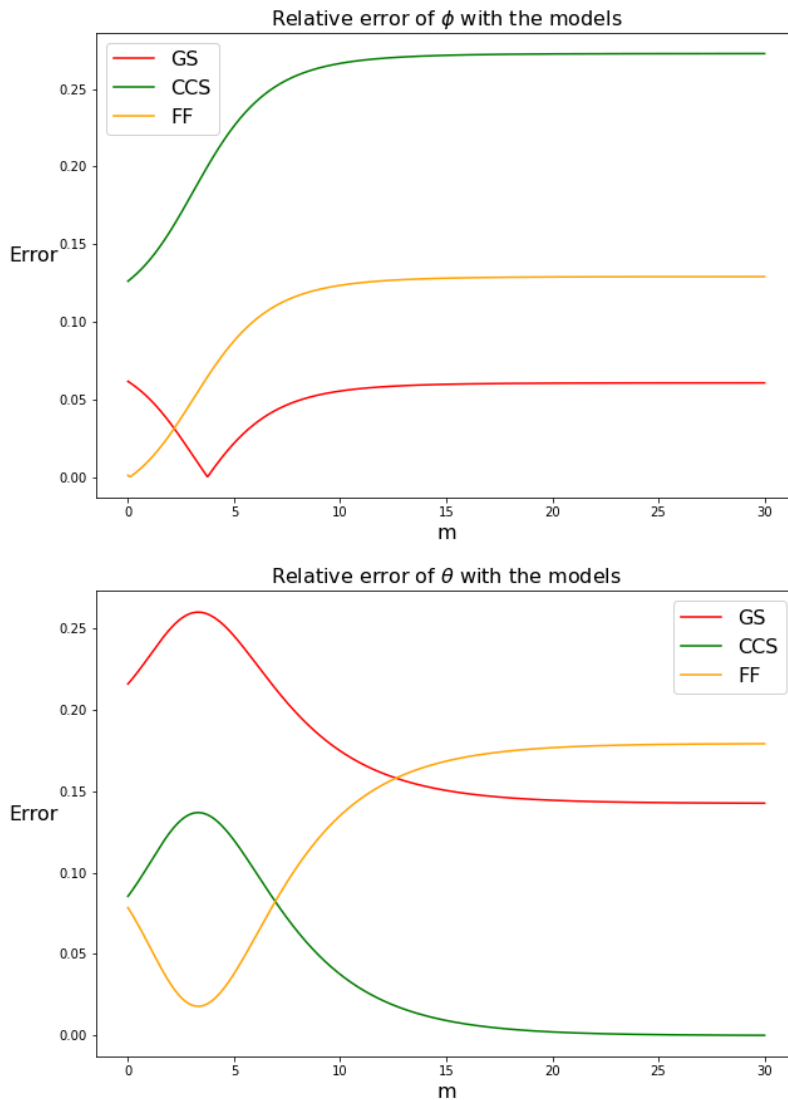
Fig. 4.13: In both panels, the red, yellow and green lines are the error profiles (ratio of the difference over the results of Al-HAddad) of the weighted averaged angles (for each degree of *m*) with respect to the GS, FF and CCS results of Al-Haddad, respectively.

4.4.2 The influence of the boundary selection

Figure 4.14 tells us that the influence of the boundary selection on the reconstruction does not strongly depends on the smoothing. Indeed, the tilts of the red curves in figure 4.11 and 4.14 are almost similar.

Moving the front boundary modifies θ of $0.66°$ min^{-1} and ϕ of $0.02°$ min^{-1}. A change in the rear boundary shifts θ by $0.16°$ min^{-1} and ϕ by $0.02°$ min^{-1}. While the choice of the front boundary seems to have a greater impact on the reconstruction, once again, the range of the rear boundary is much greater than the front one. As a quick example, for the cloud on 2013-06-28, the front boundary range stretches over 180 minutes. The rear boundary

range covers 750 minutes. Then, θ and ϕ vary with 120 degrees and 4 degrees, respectively, due to the uncertainty in the location of the front boundary. On the other hand, the maximal change in the rear boundary implies a change of 120 degrees for θ and 15 degrees for ϕ. In this example, the rear boundary has a greater impact on the ϕ angle, while both boundaries potentially change the θ angle with the same strength.

All in all, we calculated angles of $\phi = -65$ and $\theta = 330$. These results agree with the results of Al-Haddad with an average accuracy of 99.3%. The code allows us to give additional information about the cloud: The center of the torus is located at a distance of 0.838 AU of the spacecraft. The spacecraft approaches the center of the flux rope to a minimal distance of 0.017 AU. The intensity of the magnetic field in the z direction reaches up to -11.4 nT. Lastly, the poloidal flux overcomes the toroidal flux by a factor of 3.5 with a value of $F_{pol} = 1.7\ 10^{13}$ T m^2.
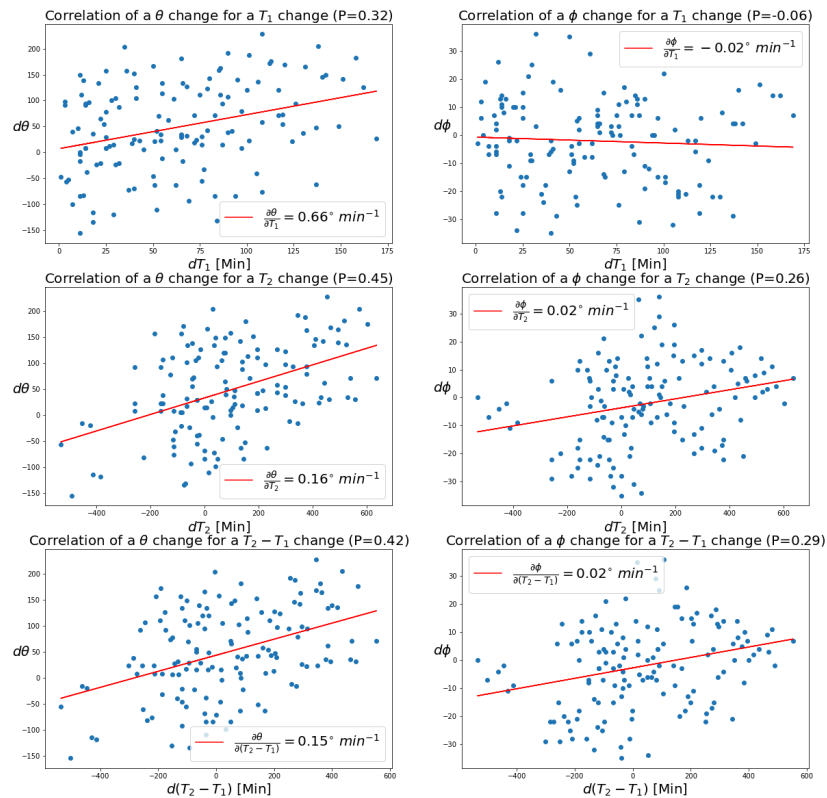
Fig. 4.14: The first column of plots concerns the variable θ. The second column concerns ϕ. The first, the second and the third lines plot the differences in the angles with respect to the differences on the front boundary, rear boundary and cloud duration, respectively. The red curves are the fitting curves of the data points. The legends display the tilt of the curve in the unit degrees per minute. P is the Pearson correlation coefficient.

4.5 Influence of the manual pick

Once the code is yielding the residue map for the Z-axis orientation, the user has to select the best angle by hand. The goal of this section is to determine the influence of that choice on the quality of the reconstruction and on the cloud's parameters.

In order to study the robustness of the code, we will fix the boundaries of the cloud. 179:04:25 (DOY:H:Min) is going to be the starting date, and 1:07:25 (D:H:Min) the duration. Smoothed data gives better accuracy. The data is smoothed over 2 hours periods. For this configuration, the relation between the eigenvalues of B_1, B_2 and B_3 are $\frac{\lambda_x}{\lambda_y} = 4$ and $\frac{\lambda_x}{\lambda_z} = 121$. These relations mean that the magnetic field rotates within these boundaries.

Table 4.8 summarizes the results of our reconstructions. The angles are those that we selected manually. The other parameters ($B_{max}, F_{pol}, \chi^2, Q, R_f$), are the outputs of the reconstructions with their respective angles. Note that once the angles are chosen, the other outputs do not depend on the user of the code.
It is important to mention that the angles have been chosen within the minimum residues islands. It explains the wide range of the θ angle and the restricted one of the ϕ angle.

$N°$	ϕ	θ	B_{max}	F_{pol}	χ^2	Q	R_f
Unit	°	°	(nT)	$(10^{13}T.m^{-2})$	x	x	x
1	−80	425	−11.39	2.31	0.433	0.999	0.07
2	−75	488	−11.71	2.99	0.453	0.999	0.05
3	−80	273	−11.24	2.03	0.474	0.998	0.06
4	−78	459	−11.5	2.57	0.456	0.999	0.06
5	−75	246	−11.5	3.64	0.424	0.999	0.06
6	−64	297	−11.77	0.668	0.464	0.998	0.11
7	−80	225	−11.55	3.95	0.608	0.962	0.05
$< x >$	−76	344	−11.52	2.6	0.473	0.993	0.07

Table 4.8: Results of seven test reconstructions to determine the influence of the manual pick in the new code of Qiang Hu. The line labeled with $< x >$ is the average of the studied variables.

4.5.1 Study of the robustness with a linear fit

Figures 4.15 and 4.16 are, respectively, the impacts of the choice of the angles ϕ and θ on some of the reconstruction parameters i.e $B_{max}, F_{pol}, \chi^2, Q, R_f$. These two figures show the robustness of the code to a change in the choice of the Z-axis angles.
At first, recall that ϕ's maximal change is of 90 degrees. If we consider the quality parameters (R_f, χ^2, Q), the approximated percentage of change to the average is 0.05% per degree. This means that the change to the average that one can obtain is 90 times this value. We can

have, roughly, a 4.5% change to the average by selecting an arbitrary ϕ inside the minimum residue contours of the residue map. In fact, for the cloud's parameters (B_{max} and F_{pol}), we have exactly the same 4.5% change to the average.

Secondly, the angle θ can have a maximal change of 180 degrees. Indeed, the change can be positive or negative. Then, we recover the 360 degrees of the residue map. Figure 4.16 tells us that the percentage of change to the average is 0.0004% per degree. Therefore, we can estimate a potential change of 0.072% to the average.

Obviously, quick calculations on the results of table 4.8 give us an idea of how approximate these conclusions are. Indeed, the red fitting curves have a low tilt, but the data points scatter broadly around them, making our predictions unprecise. On the other hand, the test sample is far from having a statistical size. Moreover, some of the Pearson coefficients are low. A linear fit may not be the best method to analyse the robustness. This is the reason why the next section repeat the study with the bootstrapping method.
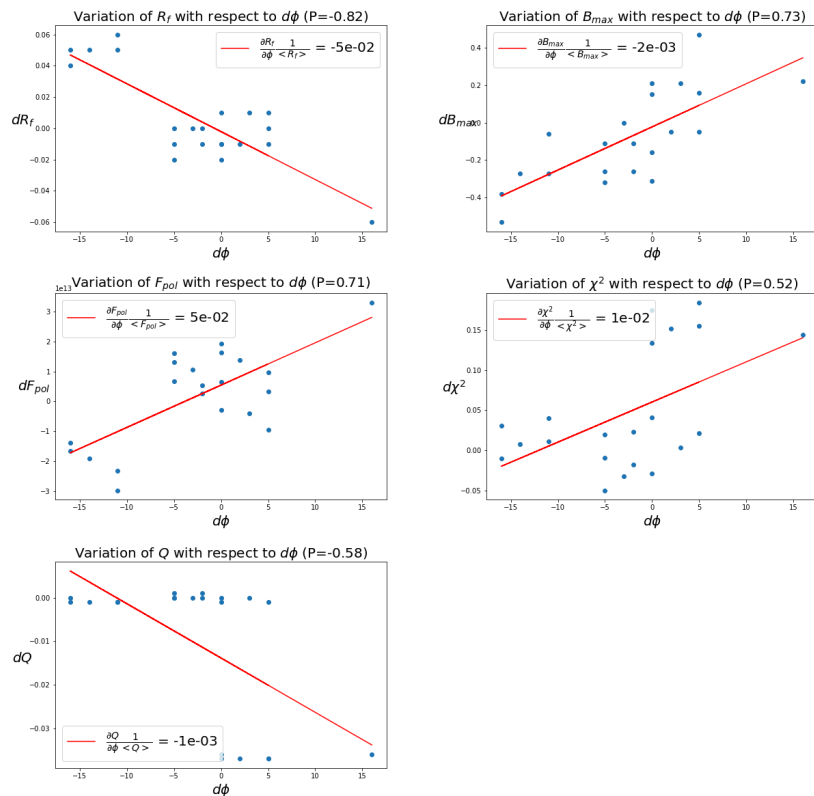
Fig. 4.15: The influences of a change of ϕ on several variables. The red lines represent the linear fits. The label of the red line displays the tilts of the red curves divided by the average of the studied value. The results can be read as a percentage of change per degree with respect to the average.
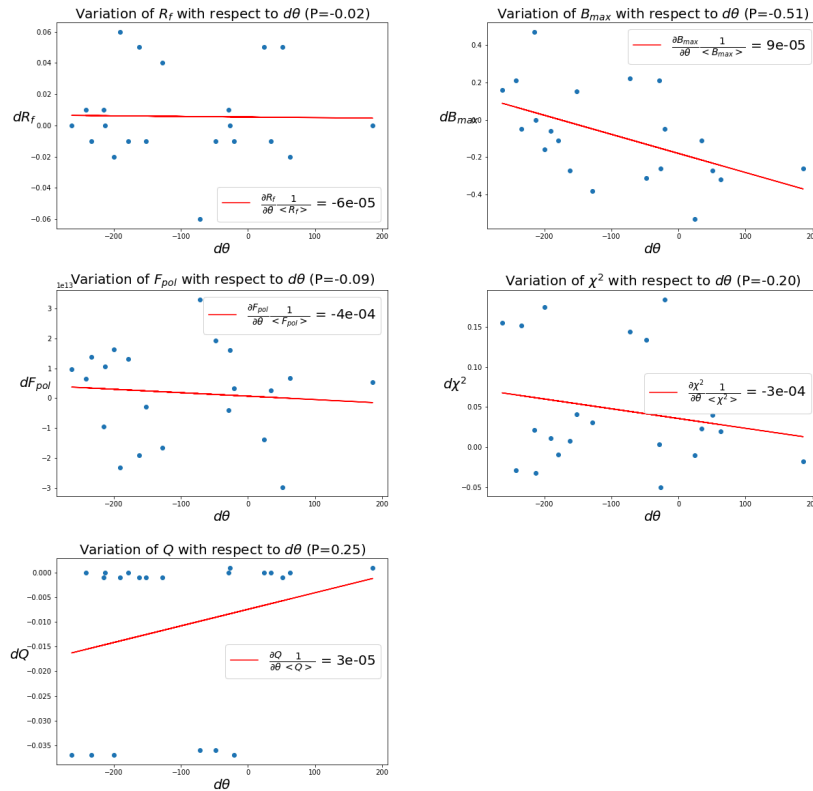
Fig. 4.16: The influences of a change of θ on several variables. The red lines represent the linear fits. The label of the red line displays the tilts of the red curves divided by the average of the studied value. The results can be read as a percentage of change per degree with respect to the average.

4.5.2 Study of the robustness with a bootstrapping method

Seven reconstructions do not represent a statistical sample, even after computing every possible combination of differences to increase the dataset. The bootstrapping method may represent an alternative to the linear fit.

The bootstrapping method consists in selecting randomly several values of a parameter and computing the mean of the selected values. This operation is repeated a large number of times. Hence, the method yields a large amount of partial mean values. These mean values are plotted as histograms.

We have seven reconstructions. All the possible combinations of differences increase the sample to $\sum_{i=1}^{7} i = 21$ values. The bootstrapping is set up to select randomly 10 values out of these 21, and to calculate the average of these 10 values. This operation is repeated 10000 times. As a result, we obtain 10000 partial mean values. These means values are plotted as in the histograms of figures 4.17 and 4.18. Finally, the total mean of the 10000 partial mean values is calculated for each parameter, normalized with the average of this parameter

(last line of table 4.8), and displayed as label "Mean" on the histograms of figures 4.17 and 4.18.
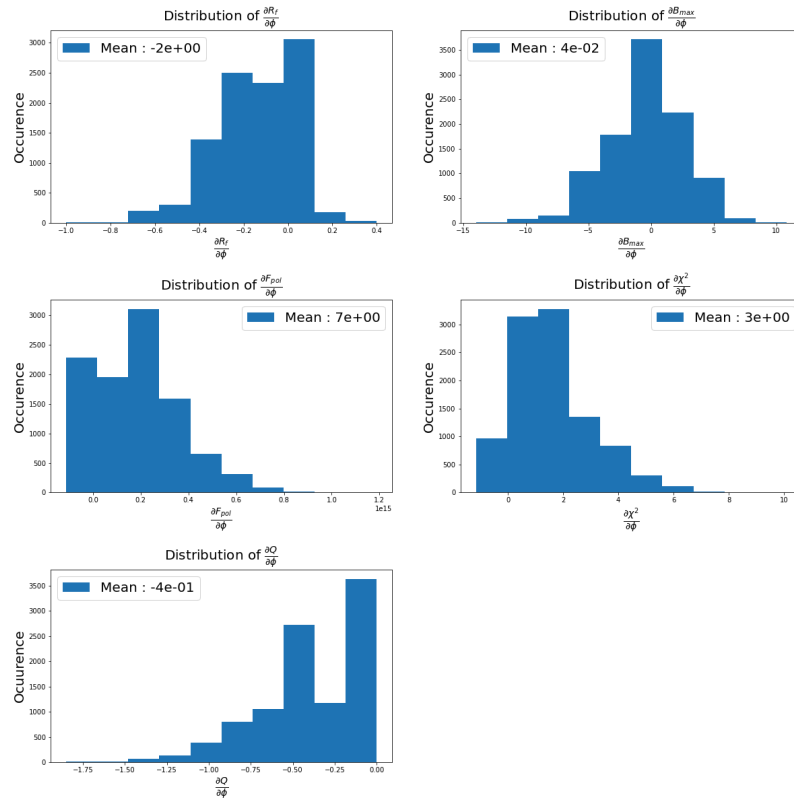
Fig. 4.17: The influences of a change of ϕ on several variables. The red lines represent the linear fits. The label of the red line displays the tilts of the red curves divided by the average of the studied value. The results can be read as a percentage of change per degree with respect to the average.

The variations of the parameters $(B_{max}, F_{pol}, \chi^2, Q, R_f)$ with respect to the angle θ are all below $4 \cdot 10^{-3}$ times their average value. The changes to the parameter's averages are below 0.4% per degree of variation of θ. As for the linear fit method, the conclusion is that the code is relatively robust under a change of θ angle.

The variations of the parameters $(B_{max}, F_{pol}, \chi^2, Q, R_f)$ with respect to the angle ϕ, however, reach up to 7 times their average value. For the parameters R_f, F_{pol}, χ^2, the changes in their average are between 200% and 700% per degrees of variation of ϕ. These changes equal 4% and 40% for the parameters B_{max} and Q respectively. Nevertheless, the Pearson coefficients for the variation in ϕ all had acceptable values with the linear fit method.

According to the bootstrapping analysis, the variation of the selection of the θ angle has a reasonable influence on the output parameters. These ones vary of few percents. However,

according to the same method, the variation of the selection of the ϕ angle has a great impact on the output parameters. The parameters vary of hundreds of percents.
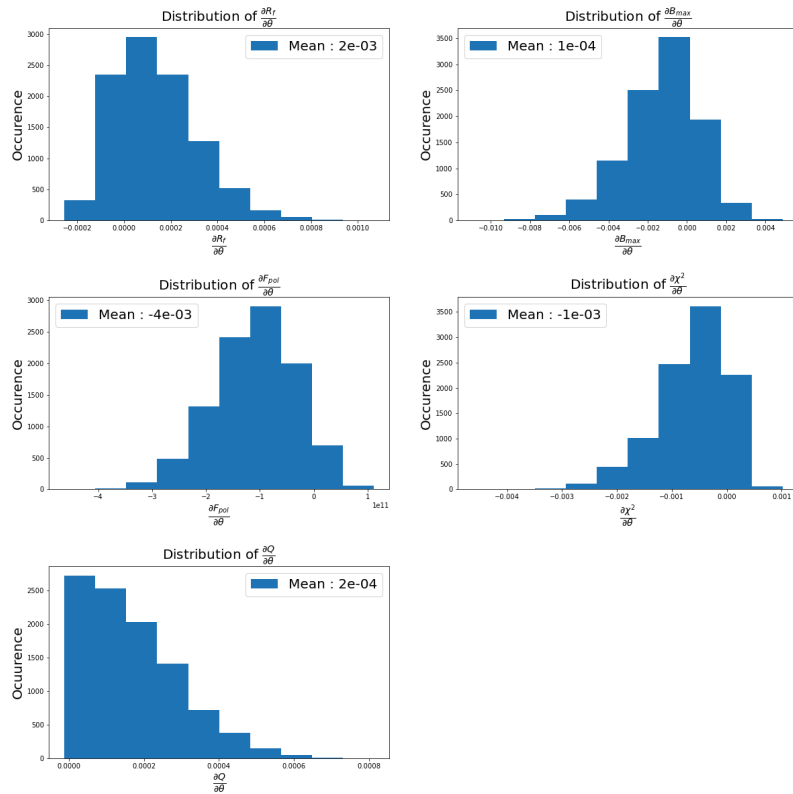
Fig. 4.18: The influences of a change of θ on several variables. The red lines represent the linear fits. The label of the red line displays the tilts of the red curves divided by the average of the studied value. The results can be read as a percentage of change per degree with respect to the average.

As a conclusion, the linear fit analysis highlights a low influence of the selection of the angles on the outputs of the reconstruction. Yet, the results of the linear fit method are not all reliable as some Pearson coefficients are low.

On the other hand, the bootstrapping method results in a greater influence of the selection of the angles on the reconstruction, especially regarding the ϕ angle.

Even though the numbers of tests are too low to provide a reliable statistical analysis, it looks like the code is robust to the choice of the Z-axis angles. Choosing the Z-axis orientation within the minimum residue contours of the residue map should provide satisfying results. This section gives even more importance to the choice of the boundaries. Indeed, if the choice on the Z-axis orientation has a limited influence on the output parameters, the choice of the boundaries has been the most important part of the reconstruction.

Conclusion

5

Magnetic flux ropes can be recognized through the rotation of the magnetic field, the linear decrease in the plasma velocity and the freeze-in of the plasma. In both events on 2004-11-09 and on 2013-06-28, the front boundaries were easier to localize than the rear boundaries. Indeed, the characteristics of flux ropes appeared clearly at the starts of the magnetic clouds, but disappeared slowly during the ends of the events. The Grad-Shafranov method is sensitive to the choice of the boundaries of the flux ropes. Nevertheless, the code of Qiang Hu, based on the Grad-Shafranov reconstruction, is able to reconstruct successfully magnetic flux ropes and retrieve the results published in the literature i.e. the articles of Isavnin et al. (2011) and Al-Haddad et al. (2018).

The study of the set of 17 reconstructions (event on 2013-06-28) gave an insight on the influence that the boundary selection has on the reconstruction of the magnetic flux ropes. A change of one minute on the front boundary changes the θ angle by $0.66°$ and the ϕ angle by $0.02°$. Whereas, a change of one minute on the rear boundary changes the θ angle by $0.16°$ and the ϕ angle by $0.02°$. However, the uncertainty of the rear boundary is more than four times greater than the uncertainty on the front one. The impact of the selection of the rear boundary becomes, thereby, greater than the impact of the front one. The duration of the cloud is almost entirely determined by the choice of the rear boundary and its study does not add substantial results. While smoothing the data did not change the influence that the boundary selection has on the reconstruction, it increased the quality parameter Q and retrieved the results of Al-Haddad et al. (2018). It appeared that the final residue R_f describes better the quality of the reconstruction in the original than in the smoothed data.

Finally, the selection of the best Z-axis orientation on the residue map of the reconstruction does not have a strong impact on the output parameters according to a linear fit on the results of seven reconstructions. However, a bootstrapping of the same results contradicts this conclusion. The latter method shows that the selection of the Z-axis orientation on the residue map has a significant impact on the output parameters of the reconstruction.

Bibliography

Al-Haddad, Nada, Teresa Nieves-Chinchilla1, Neel P. Savani, Noé Lugaz, and Ilia I. Roussev (2018). „Fitting and Reconstruction of Thirteen Simple Coronal Mass Ejections". In: *Solar Physics* (cit. on pp. 41, 43, 44, 49, 56, 65).

Antiochos, S. K., C. R. Devore, and J. A. Klimchuk (1999). „A Model For Solar Coronal Mass Ejections". In: *THE ASTROPHYSICAL JOURNAL* (cit. on p. 14).

Aschwanden, M.J, A. Winebarger, D. Tsiklauri, and H. Peter (2007). „The Coronal Heating Paradox". In: *The Astrophysical Journal, 659:1673* (cit. on p. 9).

Balogh, André, Hugh Hudson, Kristóf Petrovay, and Rudolf von Steiger (2015). *The solar activity cycle*. eng. Space sciences series of ISSI (cit. on p. 1).

Basu, Sarbani, William J. Chaplin, Yvonne Elsworth Roger New, and Aldo M. Serenelli (2009). „Fresh insights on the structure of the solar core". In: $Astrophys.J. 699 : 1403 - 1417, 2009$ (cit. on p. 6).

Bertulani, Carlos A (2013). „Nuclei in the Cosmos". In: *Texas A&M University, USA* (cit. on pp. 4, 5).

Biondo1, Ruggero, Alessandro Bemporad, Andrea Mignone, and Fabio Reale (2021). „Reconstruction of the Parker spiral with the Reverse In situ data and MHD APproach – RIMAP". In: *J. Space Weather Space Clim. 2021, 11, 7* (cit. on p. 13).

Bizzarro, James N. Connelly & Martin, Alexander N. Krot, Åke Nordlund, Daniel Wielandt, and Marina A. Ivanova (2012). „The Absolute Chronology and Thermal Processing of Solids in the Solar Protoplanetary Disk". In: *Science, Vol. 338, Issue 6107, pp. 651-655* (cit. on p. 4).

Bray, R.J (1973). „High-Resolution Photography of the Solar Chromosphere. X: Physical Parameters of H_α Mottles". In: *Solar Physics, Volume 29, Issue 2, pp.317-325* (cit. on p. 9).

Chao, J. K., Wen-Chieh Hsieh, L. Yang, and L. C. Lee (2014). „WALÉN TEST AND DE HOFF-MANN–TELLER FRAME OF INTERPLANETARY LARGE-AMPLITUDE ALFVÉN WAVES". In: *The Astrophysical Journal, Volume 786, Number 2* (cit. on p. 19).

Chen, J. (1989). „Effects of toroidal forces in current loops embedded in a background plasma". In: *Astrophysical Journal* (cit. on p. 16).

Christensen-Dalsgaard, J., W. Däppen, S.V. Ajukov, et al. (1996). „The Current State of Solar Modeling". In: $Science, 272, 1286 - 1292$ (cit. on p. 6).

Cranmer, S.N. (2009). „Coronal Holes". In: *Living Rev. Solar Phys., 6* (cit. on p. 11).

Dikpati, M. (2006). „The importance of the solar tachocline“. In: *Advances in Space Research Volume 38, Issue 5, 2006, Pages 839-844* (cit. on p. 10).

Dunbar, Brian (2017). *The NASA worldbook, The Sun*. URL: https://www.nasa.gov/sun (cit. on p. 6).

Dziembowski, W.A., G. Fiorentini, B. Ricci, and R. Sienkiewicz (1998). „Helioseismology and the solar age“. In: *A& A ,343* (cit. on p. 4).

Golub, L. and J.M. Pasachoff (2010). „The Solar Corona, second edition“. In: *Cambridge University Press* (cit. on pp. 9, 10).

Gosling, J. T., E. Hildner, R. M. MacQueen, et al. (1976). „The Speeds of Coronal Mass Ejection Events“. In: *Solar Physics* (cit. on p. 18).

Grad, H. and H. Rubin (1958). „Hydromagnetic Equilibria and Force-Free Fields“. In: *Proceedings of the 2nd UN Conf. on the Peaceful Uses of Atomic Energy, Vol. 31, Geneva* (cit. on p. 26).

Haberreiter, M., W. Schmutz, and A. G. Kosovichev (2008). „Solving the discrepency between the seismic and photospheric solar radius“. In: *The Astrophysical Journal, 675: L53–L56* (cit. on p. 4).

Habets, G. M. H. J. and J. R. W. Heintze (1981). „Empirical bolometric corrections for the main-sequence“. In: *Astronomy and Astrophysics Supplement Series, vol. 46, Nov. 1981, p. 193-237.* (cit. on p. 3).

Hathaway, Dr. David H. (2015). *The Solar Interior*. URL: https://solarscience.msfc.nasa.gov/interior.shtml (cit. on pp. 6–8).

Haverkort, J.W. (2009). „Axisymmetric Ideal MHD Tokamak Equilibria“. In: *Notes about the Grad–Shafranov equation, selected aspects of the equation and its analytical solutions.* (cit. on p. 26).

Heyvaerts, J. and E.R. Priest (1983). „Coronal heating by phase-mixed shear Alfven waves“. In: *Astronomy and Astrophysics, vol. 117, no. 2, Jan. 1983, p. 220-234* (cit. on p. 9).

Holweger, H. and E.A. Müller (1974). „The photospheric barium spectrum: Solar abundance and collision broadening of BaII lines by hydrogen“. In: *Sol Phys 39, 19–30* (cit. on pp. 8, 9).

Hu, Qiang (2016). „The Grad–Shafranov Reconstruction of Toroidal Magnetic Flux Ropes“. In: *Presentation at the Dept. Space Science, CSPAR, UAH* (cit. on p. 27).

– (2017). „The Grad–Shafranov Reconstruction of Toroidal Magnetic Flux Ropes: Method Development and Benchmark Studies“. In: *Solar Physics* (cit. on pp. 20, 24, 29, 31, 37, 38).

Isavnin, A., E.K.J Kilpua, and H.E.J Koskinen (2011). „Grad-Shafranov reconstruction of magnetic clouds: overview and improvements“. In: *Solar Physics, Volume 273* (cit. on pp. 31, 32, 35, 39, 65).

Jaschek, Carlos and Mercedes Jaschek (1987). „The Classification of Stars“. In: *The press syndicate of the University of Cambridge* (cit. on p. 3).

Jenny Mottar, NASA (2017). *Anatomy of the Sun*. URL: https://www.nasa.gov/mission_pages/sunearth/science/solar-anatomy.html (cit. on p. 7).

Jian, L. K., C. T. Russell, J. G. Luhmann, A. B. Galvin, and P. J.MacNeice (2009). „Multi-Spacecraft Observations: Stream Interactions and Associated Structures“. In: *Solar Physics, Volume 259, Issue 1-2, pp. 345-360.* DOI: 10.1007/s11207-009-9445-3 (cit. on p. 14).

Karttunen, Hannu, Pekka Kröger, Heikki Oja, Markku Poutanen, and Karl Johan Donner (2017). „Fundamental Astronomy". In: *Springer-Verlag Berlin Heidelberg* (cit. on p. 4).

Kroupa, Pavel (2000). „Solar System Exploration". In: *Monthly Notices of the Royal Astronomical Society* (cit. on p. 3).

Leblanc, F. (2011). „An introduction to stellar astrophysics". In: *John Wiley & Sons* (cit. on p. 7).

Livermore, P.W., C.B. Finlay, and M. Bayliff (2020). „Recent north magnetic pole acceleration towards Siberia caused by flux lobe elongation". In: *Nature Geoscience, Volume 13, Issue 5* (cit. on p. 21).

Lowder, Chris and Anthony Yeates (2017). „Magnetic Flux Rope Identification and Characterization from Observationally Driven Solar Coronal Models". In: *The Astrophysical Journal* (cit. on p. 1).

Luzum, B., N. Capitaine, and et al. Fienga A. (2011). „Celestial Mechanics and Dynamical Astronomy". In: *Springer, 110, 293* (cit. on p. 4).

Mamajek, E. E., A. Prsa, G. Torres, et al. (2015). „IAU 2015 Resolution B3 on Recommended Nominal Conversion Constants for Selected Solar and Planetary Properties". In: arXiv: `1510.07674 [astro-ph.SR]` (cit. on pp. 3, 4, 9).

McComas, D. J., B. L. Barraclough, H. O. Funsten, et al. (2000). „Solar wind observations over Ulysses' first full polar orbit". In: *JOURNAL OF GEOPHYSICAL RESEARCH, VOL. 105* (cit. on p. 14).

McComas, D.J., S.J. Bame, B.L. Barraclough, et al. (1998). „Ulysses' return to the slow solar wind". In: *GEOPHYSICAL RESEARCH LETTERS, VOL. 25* (cit. on p. 13).

Mitalas, R. and K. R. Sills (1992). „On the photon diffusion time scale for the sun". In: *Astrophysical Journal v.401, p.759* (cit. on p. 6).

Moore, R.L., Z.E. Musielak, S.T. Suess, and C.H. An (1991). „Alfven wave trapping, network microflaring, and heating in solar coronal holes". In: *Astrophysical Journal, Part 1 (ISSN 0004-637X), vol. 378, Sept. 1, 1991, p. 347-359* (cit. on p. 9).

Moore, R.L. and A.C. Sterling (2006). „Initiation of Coronal Mass Ejections". In: *Geophysical Monograph Series* (cit. on pp. 15, 16).

Moore, Ronald L. and Alphonse C. Sterling (2016). „Initiation of Coronal Mass Ejections". In: *NASA Marshall Space Flight Center* (cit. on p. 16).

Möstl, C., C.J. Farrugia and· H.K. Biernat and· M. Leitner·and E.K.J. Kilpua, A.B. Galvin, and J.G. Luhmann (2009). „Optimized Grad – Shafranov Reconstruction of a Magnetic Cloud Using STEREO-Wind Observations". In: *Solar Physics* (cit. on pp. 2, 31, 47).

NASA (2019). *Solar System Exploration*. URL: https://solarsystem.nasa.gov/solar-system/sun/overview/ (cit. on p. 3).

NASA, Adam Szabo, and Lynn Wilson (2021). *WIND Spacecraft*. URL: https://wind.nasa.gov/ (cit. on p. 1).

Newkirk, G.Jr. and K. Frazier (1982). „The solar cycle". In: *Physics Today, Volume 35, Issue 4, April 1982, pp.25-35* (cit. on p. 10).

Nieves-Chinchilla, T., M. G. Linton, M. A. Hidalgo, et al. (2016). „A Circular-Cylindrical Flux-Rope Analytical Model For Magnetic Clouds". In: *The Astrophysical Journal* (cit. on p. 18).

NOAA, Space Weather Prediction Center (2020). *Coronal Mass Ejections*. URL: https://www.swpc.noaa.gov/phenomena/coronal-mass-ejections (cit. on p. 18).

Ossendrijver, M. (2003). „The Solar Dynamo". In: *The Astronomy and Astrophysics Review* (cit. on pp. 10, 11).

Parker, E.N. (1958). „Dynamics of the Interplanetary Gas and Magnetic Fields". In: *Astrophysical Journal, vol. 128, p.664l* (cit. on p. 12).

Pogorelov, N. V., H. Fichtner, A. Czechowski, et al. (2016). „Heliosheath Processes and the Structure of the Heliopause: Modeling Energetic Particles, Cosmic Rays, and Magnetic Fields". In: *Space Science Reviews, Volume 212, Issue 1-2* (cit. on p. 14).

Powell, Richard (2011). *The Herzsprung Russel Diagram*. URL: http://www.atlasoftheuniverse.com/copyright.html (cit. on p. 5).

Pulkkinen, Tuija (2007). „Space Weather: Terrestrial Perspective". In: *Living Rev. Solar Phys., 4* (cit. on p. 21).

Reames, Donald V. (2000). „Particle acceleration by CME-driven shock waves". In: *NASA and Space Flight Center* (cit. on p. 17).

Riley, Pete and N. U. Crooker (2004). „KINEMATIC TREATMENT OF CORONAL MASS EJECTION EVOLUTION IN THE SOLAR WIND". In: *The Astrophysical Journal, 600:1035–1042* (cit. on p. 39).

Route, Matthew (2016). „THE DISCOVERY OF SOLAR-LIKE ACTIVITY CYCLES BEYOND THE END OF THE MAIN SEQUENCE?" In: *The Astrophysical Journal* (cit. on p. 7).

Schove, D.J. (1983). „Sunspot cycles". In: *Stroudsburg, PA, Hutchinson Ross Publishing Co. (Benchmark Papers in Geology. Volume 68), 1983, 410 p.* (cit. on p. 10).

Silverman, S. M. and E. W. Cliver (2001). „Low-latitude auroras: the magnetic storm of 14–15 May 1921". In: *U.S. Air Force Research. 4* (cit. on p. 21).

Stone, E. C., A. C. Cummings, F. B. McDonald, et al. (2005). „Voyager 1 Explores the Termination Shock Region and the Heliosheath Beyond". In: *Science, Vol. 309, Issue 5743, pp. 2017-2020* (cit. on p. 9).

Taubenschuss, Ulrich (2009). „Ideal MHD Simulation of Magnetic Clouds in the Solar Wind". In: *Karl-Franzens-Universitat Graz* (cit. on p. 15).

Thay, R. G. and R. N Thomas (1956). „Temperature Gradients in the Chromosphere". In: *Astrophysical Journal, vol. 123, p.299* (cit. on p. 9).

Verscharen, D. and K. G. Klein and· B. A. Maruca (2019). „The multi-scale nature of the solar wind". In: *Living Reviews in Solar Physics, Volume 16, Issue 1* (cit. on p. 13).

Vršnak, Bojan and Edward W. Cliver (2008). „Origin of Coronal Shock Waves". In: *Solar Physics* (cit. on p. 17).

Walker, Lisa May (2006). „Teh random walk of radiation from the sun". In: (cit. on p. 6).

Yongsheng, Ou and Xu Chao (2008). „Design and simulation of extremum-seeking open-loop optimal control of current profile in the DIII-D tokamak". In: *Plasma Physics and Controlled Fusion* (cit. on p. 30).

Zell, H. (2017). *Solar Rotation Varies by Latitude*. URL: https://www.nasa.gov/mission_pages/sunearth/science/solar-rotation.html (cit. on p. 10).

Zhang, J. and K. P. Dere (2006). „A Statistical Study of Main and Residual Accelerations of Coronal Mass Ejections". In: *The Astrophysical Journal, Volume 649, Number 2* (cit. on p. 16).

Colophon

This thesis was typeset with LaTeX 2$_\varepsilon$. It uses the *Clean Thesis* style developed by Ricardo Langner, available at http://cleanthesis.der-ric.de/. The design of the *Clean Thesis* style is inspired by user guide documents from Apple Inc.

The template was adapted by Desmond Grossmann, BSc, Stefan Janisch, BSc, Lea Schimak and Paul Beck, PhD to implement the editorial guidelines of *Astronomy & Astrophysics* and the cooperate-identity guidelines of the University of Graz for the Institute for Physics. This thesis uses the template, released on the webpage of the *Department for Geophysics, Astrophysics and Meteorology (IGAM)*[1] on *February 12, 2021*.

---

[1] https://physik.uni-graz.at/de/igam/

Declaration

Hereby I declare that I have completed this work on my own, where not explicitly mentioned otherwise, and only used the mentioned references.

Graz, May 31, 2021

Tom Eynard-Machet